*J. Fluid Mech.* (2007), *vol.* 574, *pp.* 179–207. © 2007 Cambridge University Press 
doi:10.1017/S0022112006004009 Printed in the United Kingdom

# Microscale fibre alignment by a three-dimensional sessile drop on a wettable pad

S. N. REZNIK, W. SALALHA, A. L. YARIN† AND E. ZUSSMAN

Faculty of Mechanical Engineering, Technion – Israel Institute of Technology, Haifa 32000, Israel

(Received 28 January 2005 and in revised form 28 August 2006)

Fluidic assembly provides solutions for assembling particles with sizes from nanometres to centimetres. Fluidic techniques based on patterned shapes of monolayers and capillary forces are widely used to assemble microfabrication devices. Usually, for self-assembly, the precondition is that the components must be mobile in a fluidic environment. In the present work, a shape-directed fluidic self-assembly of rod-like microstructures, such as an optical fibre on a wettable pad is demonstrated experimentally with submicrometre positioning precision. A model of the process is proposed, which accounts for the following two stages of the orientation of a fibre submerged in a sessile drop: (i) the drop melting and spreading over a wettable pad; (ii) fibre reorientation related to the surface-tension-driven shrinkage of the drop surface area. At the end of stage (ii), the fibre is oriented along the pad. The experimental results for the optical-fibre assembly by a solder joint have been compared to the modelling results, and a reasonable agreement has been found. The major outcome of the experiments and modelling is that surface tension forces on the fibre piercing a drop align the fibre rather than the flow owing to the spreading of the drop over the horizontal pad, i.e. stage (ii) mostly contributes to the alignment.

## 1. Introduction

Aligning and packaging of the individual components into larger functional blocks dominate the overall production cost of many opto-electronic devices (Boudreau 1994; Tummala 2001). In general, there are two methods for aligning optical components in an assembly: active alignment and passive alignment. Active alignment typically uses an active input light source while iteratively looking for minimum insertion loss. On the other hand, passive alignment relies on precision datum, or alternatively (by using self-assembly techniques) it relies on the surface energy of liquid droplets. The concept of fluidic self-assembly is used increasingly in many disciplines (Whitesides & Grzybowski 2002). Self-assembly is one of the few practical strategies for nanoparticles (Messer, Song & Yang 2000; Huang *et al.* 2001). Fluidic self-assembly of micromachined silicon parts on silicon and quartz substrates in a preconfigured pattern was demonstrated by Srinivasan, Liepmann & Howe (2001). In the previous works, processes based on capillary interactions between liquid drops (molten solder) and solid elements have been used to assemble electronic and mechanical structures. The examples include 'flip-chip' technology, where chips are mounted on a substrate

† Author to whom correspondence should be addressed: current address: Department of Mechanical and Industrial Engineering, University of Illinois at Chicago, 842 W. Taylor Street, Chicago, IL 60607-7022, USA; ayarin@uic.edu.

https://doi.org/10.1017/S0022112006004009 Published online by Cambridge University Press

with the help of the interconnecting materials such as metal bumps, as long as the chip surface (i.e. the active area) is facing the substrate (Lee & Basavanhally 1994; Reznik, Zussman & Yarin 2002; Salalha, Zussman & Bar-Yoseph 2004), and rotate parts of the microstructure into a non-planar orientation (Harsh, Bright & Lee 1999). In both examples, minimization of the free energy of the solder/air or water/air interfaces provides the driving force for the assembly. Solder, as well as liquid metals in general, provides a much larger driving force than such ordinary liquids as water owing to a higher surface tension. Once the chips are self-aligned, the solder joints are fixed by cooling down.

The present work demonstrates a self-assembly experiment in which a solder drop aligns a submerged short optical fibre. The fibre is initially submerged in a melted drop which wets a central part of it. Then, the drop on the fibre solidifies and is put on a horizontal rectangular pad which can be wetted by molten solder. However, initially the solder on the pad and fibre is not melted, and the fibre is not oriented along the pad axis. The process aim is to reorient the fibre in such a way that its axis will coincide with the pad centreline.

The drop is heated up until the solder melts and begins to wet the fibre and the pad (stage (i)). The drop shape becomes rather complicated, and at a certain moment the surface tension overtakes the process and shrinks the drop surface back to an equilibrium shape (stage (ii)). During stage (ii) the fibre is entrained by the molten solder drop, reoriented and eventually takes up a position parallel to the pad centreline. This is a key element of a new cost-effective method for self-assembly demonstrated with optical fibres on silicon chips. The present self-assembly method allows coarse fibre placements to be corrected automatically during the solder flow process.

The present work treats stages (i) and (ii) separately. While the melting and spreading stage (i) allows for some simple estimates, the surface-tension-driven stage (ii) requires direct numerical simulation of a three-dimensional time-dependent flow with rather complicated shapes of the free surface. Since in the present case we deal with low Reynolds numbers, the corresponding Stokes equations can be solved using the boundary element method. Dynamic self-aligning problems in two-dimensions have already been treated by this approach. However, we are unfamiliar with any three-dimensional simulation of this type. Nevertheless, some kindred situations can be found in the fully three-dimensional numerical simulations of single or multiple drops in flowing emulsions (e.g. Lowenberg & Hinch 1996; Zinchenko, Rother & Davis 1997), of elastic capsules and red blood cells in shear flows (e.g. Ramanujan & Pozrikidis 1998), or of gravitational displacement of sessile or pendant drops on inclined surfaces (Dimitrakopoulos & Higdon 1999).

The paper is organized as follows. In § 2, the experiment is described. The physical estimates for the melting and spreading stage (i) are given in § 3. The problem for the surface-tension-driven stage (ii) is posed in § 4. Non-dimensionalization is carried out in § 5. Numerical implementation is discussed in § 6. Numerical results for the three-dimensional model are presented and discussed in § 7, whereas those for the two-dimensional model are given in the Appendix. The predictions are compared with the experimental data in § 8. The conclusions are formulated in § 9.

## 2. Experimental

A short piece of optical fibre coated with a wettable layer was submerged in a drop of solder while the solder was being heated to its melting point. The fibre was withdrawn and a smaller solder drop was withdrawn on it and solidified. The optical fibre with the solidified solder drop on it was positioned on a horizontal

https://doi.org/10.1017/S0022112006004009 Published online by Cambridge University Press

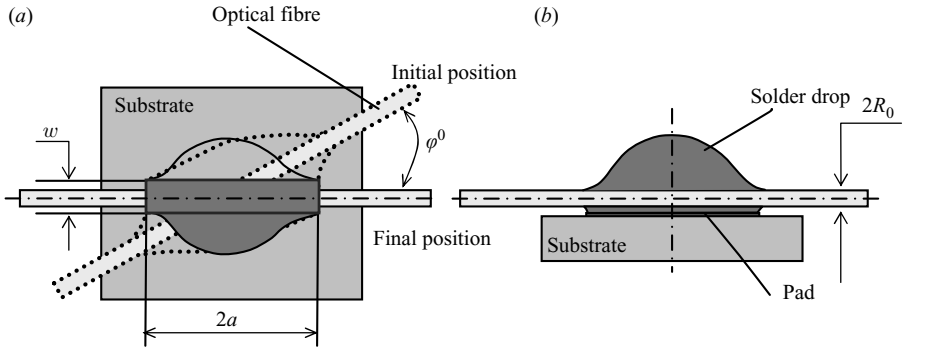



FIGURE 1. Illustration of the mechanism of the self-assembly of optical fibre by using a solder drop positioned on a rectangular horizontal wettable pad attached to a substrate. The fibre is submerged in the solder and initially misoriented at an angle $\varphi^0$ relative to the pad long centreline. At the end of the self-assembly process, the fibre should be aligned with the pad centreline, while the solder wets the entire pad and part of the fibre (the wettable area). (*a*) Top view, and (*b*) side view. The wettable pad dimensions are $w \times 2a$, and the fibre cross-sectional radius is $R_0$.

rectangular wettable pad mounted on a substrate (figure 1). The fibre was initially misoriented by an angle $\varphi^0$ relative to the long centreline of the pad. Then the substrate was heated. When the substrate had reached the temperature required to melt the solder, the solder drop started spreading over the pad and the entire wettable layer on the fibre. This was followed by fibre reorientation toward the pad centreline. The experiments were observed by an optical microscope (Olympus BX51) and a CCD camera (MotionScope PCI 8000S) at 250 f.p.s. Substrates were made of silicon chips with various pad dimensions deposited on them. A typical pad geometry was rectangular (widths $w = 0.2, 0.3, 0.4$ mm and lengths $2a = 2, 3, 4$ mm). The pads were manufactured via metallization of three layers: an adhesion layer, a wetting layer and an oxidation-barrier layer. The adhesion layer consisted of chromium/copper ($\sim$0.5 μm). The function of this layer was to form a strong bond with the silicon chip. The wetting layer was made of copper and nickel ($\sim$1.5 μm) which must remain at least partially intact throughout the assembly process. The oxidation-barrier layer ($\sim$0.1 μm) was made of gold which protected the copper from oxidation. Liquid material was solder (eutectic Pb37Sn63), which melts in the range 180–200 °C having density $\rho = 13\,\mathrm{g\,cm^{-3}}$, viscosity $\mu$ in the range $10$–$10^2\,\mathrm{g\,cm^{-1}\,s^{-1}}$ and surface tension $\sigma = 480\,\mathrm{dyn\,cm^{-1}}$. The drop had a typical volume of $0.7 \times 10^{-3}$–$1.2 \times 10^{-3}\,\mathrm{cm^3}$. The optical fibres used in the present work were soaked in water: hydrogen fluoride (1 : 10) solution for 1 h to clean them, and then rinsed in water and dried. After that they were metallized with the same materials as those of the pad using a special deposition system, and had a typical length of 1–5 cm and an outer diameter of $2R_0 = 125$ μm. The drop size $d_0 = 2a_0 \simeq 10^{-1}$ cm was much smaller then the fibre length $2l_0 = 1$–5 cm and most of the fibre protruded from the drop.

Two major stages of the process have been distinguished during the fibre self-assembly: (i) solder melting and spreading over the pad and the fibre; (ii) fibre alignment by the restoring force resulting from the surface tension. The duration of the melting and spreading stage (i) was found to be of the order of 1–3 s. During this time, the solder melted and the drop spread over the pad and the fibre. Only after that did stage (ii) begin. Then the forces resulting from the surface tension rapidly rotated the fibre toward the pad centreline. This stage lasted about 30 ms. During

https://doi.org/10.1017/S0022112006004009 Published online by Cambridge University Press

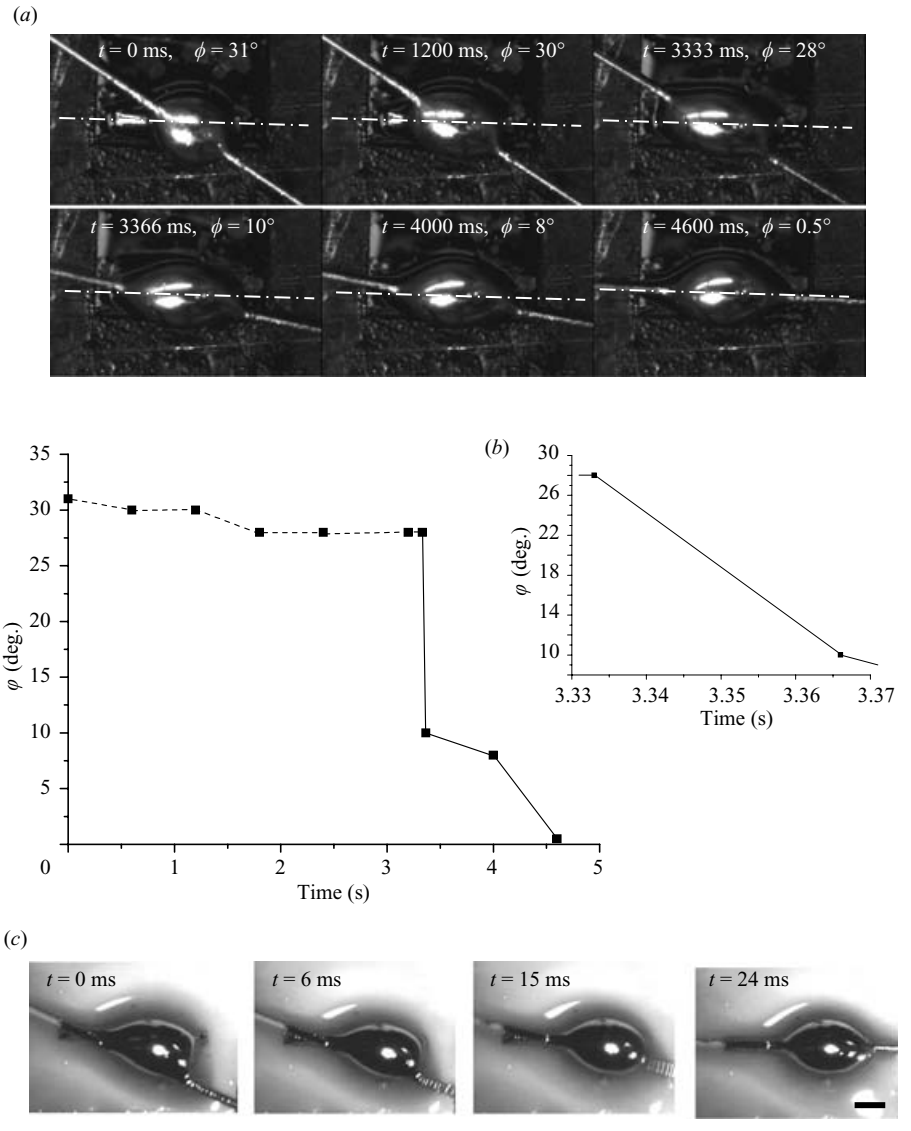



FIGURE 2. (*a*) Top view of the process taken by the CCD camera, which illustrates the mechanism of the optical fibre self-assembly (spreading and surface-tension-driven) on a longitudinal pad. The pad dimensions: $w \times 2a = 0.4 \times 4\,\mathrm{mm}^2$, the solder volume: $0.67\,\mathrm{mm}^3$, and the fibre length 3 cm. The bar in the figure is 1 mm. (*b*) The angle $\varphi$ between the fibre and the pad centrelines versus time. Symbols, experimental data. The dashed-dotted line, stage (i); the solid line, stage (ii). The insert shows in detail stage (ii) which lasts about 30 ms. (*c*) Surface-tension-driven fibre alignment, stage (ii). Pad dimensions $w \times 2a = 0.4 \times 4\,\mathrm{mm}^2$, solder volume: $0.67\,\mathrm{mm}^3$. The fibre length was 3 cm. Top view of the alignment process taken by the CCD camera (at 250 f.p.s.). Time is reckoned from the beginning of stage (ii). The bar in the figure is 1 mm.

stage (ii), solder contact lines on the pad and fibre were practically arrested, which is discussed in detail in § 4.

After the fibre was self-assembled, the final angle of the fibre centreline relative to the pad centreline was measured; the average misalignment angle of 20 experiments was $0.1^\circ \pm 0.1^\circ$. Figure 2(*a*) shows the photographic sequence of the fibre alignment

https://doi.org/10.1017/S0022112006004009 Published online by Cambridge University Press

process, whereas figure 2(*b*) shows the angle $\varphi$ between the fibre and the pad centrelines during the whole process versus time. The melting and spreading stage (i), according to figure 2(*b*), lasted about 3.3 s and the angle $\varphi$ decreased by about 5°. Then the surface-tension-driven stage (ii), when the drop rapidly minimizes its surface energy, has begun. It lasted about 36 ms. During this time, the angle $\varphi$ decreased by about 17°. Then the fibre motion was slowed down by contamination of the surfaces and/or by the fibre friction at the pad. It took about 1 s before the fibre finally aligned itself along the pad centreline. In figure 2(*b*), the dashed line traces the characteristic melting/spreading stage (i), and the surface-tension-driven stage (ii) is shown by the solid line.

Figure 2(*c*) shows stage (ii) for one of the solder drops studied experimentally. The duration of stage (ii) in all cases was of the order of $10^2$ ms. The effect of the solder volume was, however, difficult to quantify, since the thermal prehistory of stage (ii) differs for different drops. Figure 2(*c*) shows that perfect alignment of the fibre along the pad had been achieved. The experimental data on the dependence $\varphi = \varphi(t)$ during stage (ii) is presented in § 8 where it is compared to the theoretical predictions.

In additional experiments, drop spreading on a pad was studied without the submerged fibre. In this case, the pad was mounted on a glass slide, and a solidified solder drop was positioned on it. The spreading of the drops was captured from the moment they started to melt. The drops were back lit. With this method, we were able to capture 150 images of the spreading drop per second. From each consecutive image, the edge of the drop and its reflection were located with a common Sobel edge detector using Matlab software. With this arrangement it was possible to measure drop base position $Y(t)$, directly over a long period of time with high resolution. We also measured the spreading of silicone oil on the pad. A needle of a syringe containing the liquid was fixed just above the substrate, so that a drop released from the tip of the needle immediately touched the solid surface and began to spread.

## 3. Physical estimates for stage (i)

The thermal situation inside a solder drop with inserted fibre deserves a separate evaluation. Taking the thermal diffusivity of solder as that of lead, $\alpha_l = 0.2343\,\mathrm{cm^2\,s^{-1}}$, and the characteristic size of the order of the drop size $d_0 = 0.1$ cm, the characteristic time of solder melting $\tau_l = d_0^2/\alpha_l = 4.27 \times 10^{-2}$ s, which is much shorter than the characteristic time of the process of the order of several seconds following from figure 2. This might imply that the whole sequence shown in figure 2 is fully isothermal, with solder being liquid. However, this is not the case. Indeed, taking for the estimate of the thermal diffusivity of the glass fibre $\alpha_g = 3.4 \times 10^{-3}\,\mathrm{cm^2\,s^{-1}}$, the characteristic time of heating of the part of the fibre submerged near the drop top appears to be $\tau_g = d_0^2/\alpha_g = 2.94$ s. (The length of the submerged part of the fibre is of the order of $d_0$, and it is in contact with the cold protruding parts of the fibre. Therefore, $d_0$ rather than $2R_0$ is used as a length scale). This indicates that solder in contact with the fibre continues to be mostly solid, even though the drop bottom in contact with the pad has already been melted and flows (spreads over the pad) practically from the beginning of the process. Therefore, the fibre frozen into a solid 'iceberg' initially can be oriented only owing to the alignment of the whole solid top (almost like the barrel of a tank's turret) as a result of the spreading of the molten sublayer over the pad. Only after the 'iceberg' around the fibre fully melts, does surface tension fully come into play, minimizing the surface energy, and major fibre reorientation occurs. This conclusion was corroborated by the following experiment. An optical fibre with a solidified solder drop on it was heated up to 170 °C (which is close to the melting

https://doi.org/10.1017/S0022112006004009 Published online by Cambridge University Press

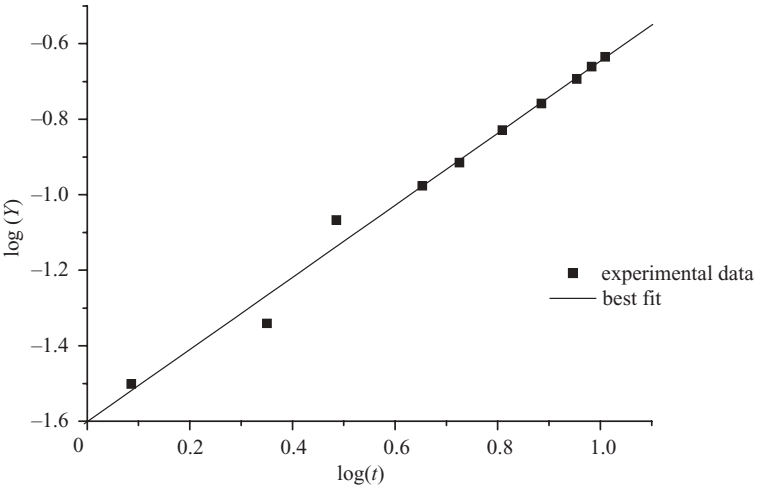



FIGURE 3. A typical graph presenting the spreading rate of the drop base coordinate, $Y(t)$, on a pad ($w \times 2a = 0.3 \times 3\,\mathrm{mm}^2$). In this case $\mathrm{d}\log(Y)/\mathrm{d}\log(t) \sim 0.91$ (with standard deviation of 0.122). The solder drop volume was $3.35 \times 10^{-5}\,\mathrm{cm}^3$.

point of the solder). Then, it was rapidly deposited on a preheated pad. Therefore, the solder in contact with the wetted part of the fibre was molten from the very beginning and the entire solder drop reached thermal equilibrium much faster then in figure 2. As a result, the subdivision of the dependence $\varphi = \varphi(t)$ into two stages (i) and (ii) practically disappeared, and the decrease of the angle $\varphi$ was gradual, lacking the abrupt fall visible in figure 2(*b*).

The additional experiments showed that, in the present case, spreading of molten solder follows neither the planar Tanner's law for the contact line coordinate $Y \sim t^{1/7}$, nor the axisymmetric Tanner's law $Y \sim t^{1/10}$ (Tanner 1979; Davis 2000); $t$ is time. For solder drops, we recorded the spreading law $Y \sim t^{0.9}$ even for the most remote part of the spreading process (an example is given in figure 3), which is a significant deviation from the results for silicone oils in the present and previous works which follow Tanner's law. For example, for a $10^{-3}\,\mathrm{cm}^3$ drop of silicon oil we measured $Y \sim t^{0.14}$ (with a very low standard deviation in the exponent value). Deviations from Tanner's law have been recorded in experiments with many low-viscosity liquids (see Drelich & Chibowska 2005 for a review). They can be partly attributed to the inertia and gravity effects which yield $Y \sim t^{1/2}$ (Reznik & Yarin 2002; Biance, Clanet & Quere 2004; Drelich & Chibowska 2005). However, for liquid metal spreading on metallized surfaces or ceramics, and, in particular, for solder spreading on metal pads, the deviation can be related to the so-called 'reactive spreading' where wettability is accompanied by dissolution of the pad metal in solder and probably by the emergence of solutal-driven Marangoni motions (Braun *et al.* 1995; Landry & Eustathopoulos 1996; Saiz & Tomsia 2004). As a result, liquid-metal reactive spreading can be faster than that of organic liquids of similar viscosity. It is worth noting, that reactive spreading is not fully understood at present.

## 4. Formulation of the problem for the surface-tension-driven stage (ii)

Major fibre reorientation occurs at stage (ii) when solder is fully melted and solder spreading over the pad and fibre is practically over. The present and the following

https://doi.org/10.1017/S0022112006004009 Published online by Cambridge University Press

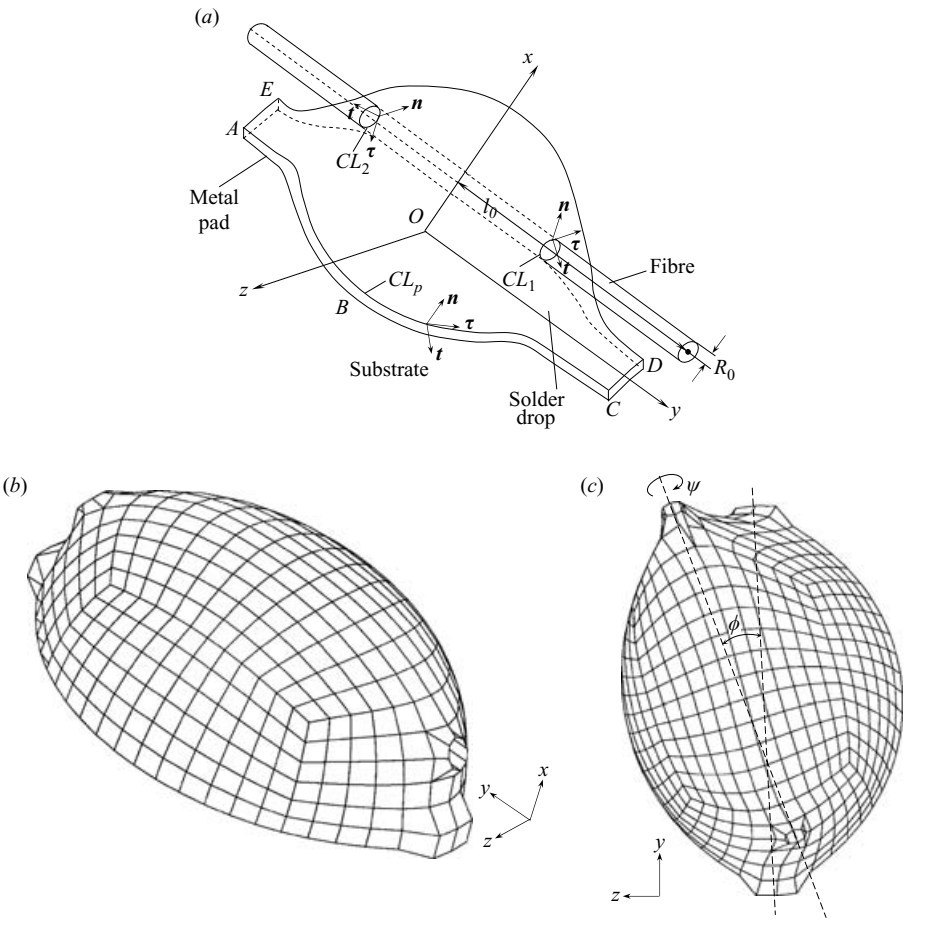



FIGURE 4. (*a*) Sketch of the three-dimensional problem. (*b*) An equilibrium drop shape at the end of stage (i), if the fibre axis were oriented parallel to the centreline of the pad. Here and hereinafter the fibre itself is not shown. (*c*) The fibre is displaced from its equilibrium position and initially rotated by the angle $\varphi = \varphi^0$ about the axis passing through its centre-of-mass parallel to the $x$-axis (top view). The contact lines are supposed to be motionless (relative to the fibre) when the fibre starts moving. The fibre is horizontal.

sections are devoted to the numerical simulation of the surface-tension-driven stage (ii). As we have seen in the experiment, this is a relatively short stage, which allows us to consider all the contact lines to be effectively arrested. Consider a solder drop of volume $V$ on a metal pad of wetted half-length $a$. A long cylindrical coated fibre of half-length $l_0$ and radius $R_0$ is placed into the drop parallel to the pad plane (but not to its centreline) so that the centre-of-mass of the fibre is located at the $x$-axis which passes through the drop centre-of-mass. Suppose that the fibre can move only parallel to the horizontal plane $y, z$ containing the pad (see figure 4*a*) with the $y$-axis directed along the pad axis. It is assumed that the solder had already spread over the pad and the coated fibre and as a result, the drop could possess an elongated shape (along the fibre and the pad) similar to the one shown in figure 4(*b*). Then this would be an equilibrium state of the fibre–drop system if the fibre were oriented parallel to the pad axis. Initially, however, the fibre is displaced from it. The centre-of-mass of the fibre can be displaced parallel to the plane $y, z$, while it is rotated by an angle

https://doi.org/10.1017/S0022112006004009 Published online by Cambridge University Press

$\varphi^0$ about the $x$-axis (see figure 4$c$). After that, the drop–fibre system evolves mostly under the action of capillary and viscous forces. The system tends to have a minimal solder surface area for a fixed volume $V$, and then the fibre moves, while all the contact lines on the pad and fibre are arrested at the positions reached at the end of the stage (i). We shall examine the time evolution of the drop and the corresponding motion of the fibre.

Let us estimate the characteristic Reynolds number for this problem. We take the solder density $\rho \sim 10\,\mathrm{g\,cm^{-3}}$, the viscosity $\mu \sim 10\,\mathrm{g\,cm^{-1}\,s^{-1}}$, the characteristic length scale of the drop $d_0 \leqslant 0.1\,\mathrm{cm}$, the surface tension coefficient $\sigma \sim 100\,\mathrm{g\,s^{-2}}$, the velocity scale $V_0 = \sigma/\mu \sim 10\,\mathrm{cm\,s^{-1}}$ (in reality the characteristic velocity is much lower, of the order of $10^{-2}\sigma/\mu \sim 10^{-1}\,\mathrm{cm\,s^{-1}}$). Then the Reynolds number is

$$Re = \frac{\rho V_0 d_0}{\mu} \leqslant 1. \tag{1}$$

The above estimate enables us to disregard the minor inertial effects in the drop, and to consider the problem in the framework of the creeping flow approximation. The Stokes equations read

$$\nabla p = \mu \Delta \boldsymbol{u}, \tag{2}$$

$$\nabla \cdot \boldsymbol{u} = 0, \tag{3}$$

where the velocity vector $\boldsymbol{u} = (u_x, u_y, u_z)$ ($u_x, u_y, u_z$ being its $x$, $y$ and $z$-components), $p$ is the pressure.

The dynamic boundary conditions at the drop surface consist in vanishing of the tangential stresses and in the normal stress balance accounting for the effect of surface tension, namely

$$\boldsymbol{f} = \sigma \kappa \boldsymbol{n}, \tag{4}$$

$$f_i = \Pi_{ik} n_k, \quad i, k = \{x, y, z\}, \tag{5}$$

$$\Pi_{ik} = -p\delta_{ik} + \mu \left( \frac{\partial u_i}{\partial x_k} + \frac{\partial u_k}{\partial x_i} \right), \tag{6}$$

where $\boldsymbol{f}$ is the traction acting at the liquid surface; $\Pi_{ik}$ are the components of the stress tensor; $\boldsymbol{n}$ is the unit outward normal vector at the surface; $\kappa$ is the surface mean curvature.

The kinematic boundary condition at the surface reads

$$\frac{\mathrm{d}\boldsymbol{r}_i}{\mathrm{d}t} = \boldsymbol{u}(\boldsymbol{r}_i), \tag{7}$$

where $\boldsymbol{r}_i$ is the position vector of the $i$th material point at the surface at time $t$.

Since all the contact lines are assumed to be arrested, the boundary conditions at the pad and the fibre surface express the no-slip condition and read

$$\boldsymbol{u} = 0, \quad \boldsymbol{r} \in \text{pad surface}, \tag{8}$$

$$\boldsymbol{u} = \boldsymbol{U}(\boldsymbol{r}), \quad \boldsymbol{r} \in \text{fibre surface}, \tag{9}$$

where $\boldsymbol{U}(\boldsymbol{r})$ is the velocity distribution over the fibre surface, determined by its motion as a rigid body. In fact, we assume that the shape of the drop base corresponds to the complicated configuration $ABCDE$ shown in figure 4($a$), i.e. some preliminary drop spreading over the borders $AC$ and $DE$ of the pad is allowed for, and points similar to $B$ are located on the substrate outside the pad, as happens in reality

https://doi.org/10.1017/S0022112006004009 Published online by Cambridge University Press

even on hydrophobic substrates (Gau *et al.* 1999) and in the present experiments (cf. figures 2*a* and 3).

The fibre position is determined by the coordinates of its centre-of-mass $\boldsymbol{r}_{cm} = (x_{cm}, y_{cm}, z_{cm})$ (in our case $x_{cm} = \text{const}$), and two angles: the angle between the pad and the fibre centrelines $\varphi$; and the angle of the fibre rotation about its own axis $\psi$ (see figure 4*c*). The velocity of the centre-of-mass of the fibre $\boldsymbol{u}_{cm}$ and the fibre angular speed $\boldsymbol{\omega}$ can be represented as

$$\boldsymbol{u}_{cm} = (0, V_y, V_z), \quad \boldsymbol{\omega} = (\omega_\varphi, \omega_\psi \cos\varphi, \omega_\psi \sin\varphi), \tag{10}$$

where $\omega_\varphi$ is the angular speed of the fibre rotation about the $x$-axis, and $\omega_\psi$ is the angular speed of rotation about the axis of the fibre.

The equations of motion of the fibre read

$$m\frac{\mathrm{d}V_y}{\mathrm{d}t} = F_y, \tag{11}$$

$$m\frac{\mathrm{d}V_z}{\mathrm{d}t} = F_z, \tag{12}$$

$$I_x\frac{\mathrm{d}\omega_\varphi}{\mathrm{d}t} = M_x, \tag{13}$$

$$I_0\frac{\mathrm{d}\omega_\psi}{\mathrm{d}t} = M_y\cos\varphi + M_z\sin\varphi, \tag{14}$$

$$\frac{\mathrm{d}y_{cm}}{\mathrm{d}t} = V_y, \tag{15}$$

$$\frac{\mathrm{d}z_{cm}}{\mathrm{d}t} = V_z, \tag{16}$$

$$\frac{\mathrm{d}\varphi}{\mathrm{d}t} = \omega_\varphi, \tag{17}$$

$$\frac{\mathrm{d}\psi}{\mathrm{d}t} = \omega_\psi, \tag{18}$$

where $F_y$, $F_z$ are the components of the force exerted on the fibre by the drop, $M_x$, $M_y$, $M_z$ are the components of the moment of force relative to the centre-of-mass of the fibre exerted by the drop on the fibre, $I_x$ is the moment of inertia of the fibre relative to the axis, going through its centre-of-mass and parallel to the $x$-axis, $I_0$ is the moment of inertia of the fibre relative to its own axis. The velocity $\boldsymbol{U}(\boldsymbol{r})$ is related to $\boldsymbol{r}_{cm}$, $\boldsymbol{u}_{cm}$ and $\boldsymbol{\omega}$ as

$$\boldsymbol{U} = \boldsymbol{u}_{cm} + \boldsymbol{\omega} \times \widetilde{\boldsymbol{r}}, \tag{19}$$

where $\widetilde{\boldsymbol{r}} = \boldsymbol{r} - \boldsymbol{r}_{cm}$.

Even though the glass fibre density is less than that of the solder and flow of the latter is considered to be inertialess, the inertia of the fibre should be accounted for since, in many cases, fibres can protrude from the drop, and only a small part of them is submerged.

To determine the force $\boldsymbol{F}$ and the moment of force $\boldsymbol{M}$, note that the overall force and the moment exerted on the inertialess drop should be equal to zero:

$$\oint_\Gamma \boldsymbol{f}\,\mathrm{d}S = 0, \quad \oint_\Gamma \boldsymbol{r} \times \boldsymbol{f}\,\mathrm{d}S = 0, \tag{20}$$

https://doi.org/10.1017/S0022112006004009 Published online by Cambridge University Press

where $\Gamma$ is the overall liquid surface including that of the bottom in contact with the pad and substrate. Using the boundary condition (4), we find

$$\int_{pad+substrate} \boldsymbol{f}\,\mathrm{d}S + \int_{fibre} \boldsymbol{f}\,\mathrm{d}S + \sigma \int_{\widetilde{\Gamma}} \kappa \boldsymbol{n}\,\mathrm{d}S = 0, \tag{21}$$

$$\int_{pad+substrate} \widetilde{\boldsymbol{r}} \times \boldsymbol{f}\,\mathrm{d}S + \int_{fibre} \widetilde{\boldsymbol{r}} \times \boldsymbol{f}\,\mathrm{d}S + \sigma \int_{\widetilde{\Gamma}} \kappa \widetilde{\boldsymbol{r}} \times \boldsymbol{n}\,\mathrm{d}S = 0, \tag{22}$$

where $\widetilde{\Gamma}$ is the drop free surface and $\boldsymbol{f}$ denotes tractions at the surfaces. The third terms in (21) and (22) can be expressed as

$$\int_{\widetilde{\Gamma}} \kappa \boldsymbol{n}\,\mathrm{d}S = \oint_{CL_1} \boldsymbol{t}\,\mathrm{d}l + \oint_{CL_2} \boldsymbol{t}\,\mathrm{d}l + \oint_{CL_p} \boldsymbol{t}\,\mathrm{d}l, \tag{23}$$

$$\int_{\widetilde{\Gamma}} \kappa \widetilde{\boldsymbol{r}} \times \boldsymbol{n}\,\mathrm{d}S = \oint_{CL_1} \widetilde{\boldsymbol{r}} \times \boldsymbol{t}\,\mathrm{d}l + \oint_{CL_2} \widetilde{\boldsymbol{r}} \times \boldsymbol{t}\,\mathrm{d}l + \oint_{CL_p} \widetilde{\boldsymbol{r}} \times \boldsymbol{t}\,\mathrm{d}l, \tag{24}$$

where $CL_1$ and $CL_2$ are the contact lines between the liquid and the fibre, $CL_p$ is the contact line between the liquid and the pad and substrate. Also $\boldsymbol{t} = \boldsymbol{\tau} \times \boldsymbol{n}$, where $\boldsymbol{\tau}$ is the unit tangent vector to a contact line, and $\boldsymbol{n}$ is the unit outer normal vector to the drop surface (see figure 4*a*). Substituting (23) and (24) into (21) and (22), respectively, and denoting the total traction acting on the fibre from the drop by $\boldsymbol{F}$, and the total moment of force acting on the fibre from the drop by $\boldsymbol{M}$, we obtain

$$\begin{aligned} \boldsymbol{F} &= -\int_{fibre} \boldsymbol{f}\,\mathrm{d}S - \sigma \left( \oint_{CL_1} \boldsymbol{t}\,\mathrm{d}l + \oint_{CL_2} \boldsymbol{t}\,\mathrm{d}l \right) \\ &= \int_{pad+substrate} \boldsymbol{f}\,\mathrm{d}S + \sigma \oint_{CL_p} \boldsymbol{t}\,\mathrm{d}l, \end{aligned} \tag{25}$$

$$\begin{aligned} \boldsymbol{M} &= -\int_{fibre} \widetilde{\boldsymbol{r}} \times \boldsymbol{f}\,\mathrm{d}S - \sigma \left( \oint_{CL_1} \widetilde{\boldsymbol{r}} \times \boldsymbol{t}\,\mathrm{d}l + \oint_{CL_2} \widetilde{\boldsymbol{r}} \times \boldsymbol{t}\,\mathrm{d}l \right) \\ &= \int_{pad+substrate} \widetilde{\boldsymbol{r}} \times \boldsymbol{f}\,\mathrm{d}S + \sigma \oint_{CL_p} \widetilde{\boldsymbol{r}} \times \boldsymbol{t}\,\mathrm{d}l. \end{aligned} \tag{26}$$

The expressions (25) and (26) mean that, for the inertialess drop, the force and the moment of force acting on the fibre from the drop are equal, with the opposite sign to those acting on the pad and substrate. Therefore, $\boldsymbol{F}$ and $\boldsymbol{M}$ can be calculated, in principle, either using the tractions at the fibre surface (the middle expressions in (25) and (26)), or those at the pad surface (on the right-hand sides in (25) and (26)).

In the general case, the contact lines $CL_1$ and $CL_2$ can move over the fibre surface. Then, singularities of stresses and vorticity at the moving contact line would appear if the no-slip conditions (9) are implemented at the fibre surface (Dussan 1979; Kistler 1993). Then, the question of how to calculate the forces and moments exerted on the fibre using (25) and (26) arises. Since the transitional zones between the regions near the contact lines on the fibre surface are expected to be much smaller than the cross-sectional radius of the fibre, we neglect the curvature of the latter and consider it as being plane. To remove the singularities near the moving contact lines, various models were proposed. For example, in Cox (1986) and Hocking (1977), a slip model was used. The force acting on a planar surface was calculated for some simple cases in Hocking (1977). According to Cox (1986) the contact angle at the close vicinity of the contact line is equal to its stationary value $\alpha_s$. The small transition zone exists

https://doi.org/10.1017/S0022112006004009 Published online by Cambridge University Press

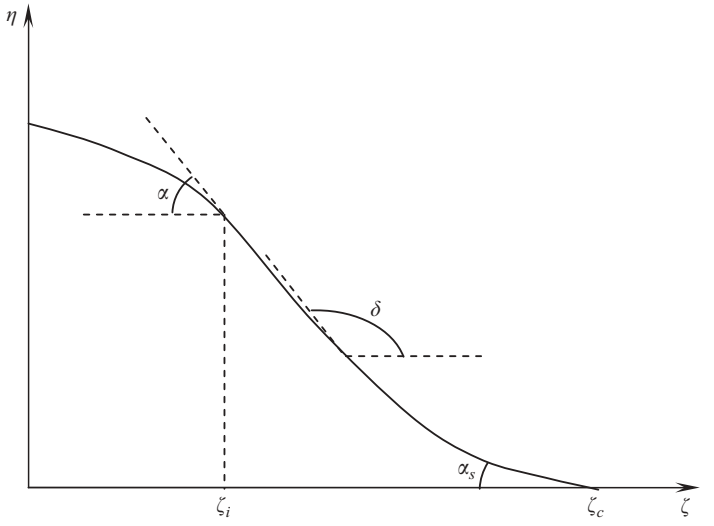



FIGURE 5. Sketch of the free surface near a solid surface (of the fibre or the pad and substrate) directed along the $\zeta$-axis (the transition zone).

where the slope angle of the surface changes its value from $\alpha_s$ to the apparent contact angle $\alpha$. Then the surface traction can be represented as follows,

$$\boldsymbol{f} = \boldsymbol{f}^0 + U_{cl}\,\boldsymbol{f}^u, \tag{27}$$

where $U_{cl}$ is the contact line velocity, $\boldsymbol{f}^0$ is the non-singular part of the traction which would exist in the case when the contact line is fixed, and $\boldsymbol{f}^u$ is related to the CL motion, responsible for the changing of the slope angle of the free surface in the transition zone from the static contact angle to the apparent one. It has a universal form corresponding to the solution of Moffatt (1964) for a wedge. Outside the transition zone, $U_{cl}\,\boldsymbol{f}^u \ll \boldsymbol{f}^0$ because of the smallness of $U_{cl}$ relative to the bulk velocities. In the transition zone, the normal stress balance is

$$\sigma\kappa = -\sigma\frac{\mathrm{d}\sin\delta}{\mathrm{d}\zeta} \approx U_{cl}\,f_n^u, \tag{28}$$

where $f_n^u$ is the normal to the liquid surface component of $\boldsymbol{f}^u$, $\delta$ is the slope angle of the surface. Then, if we want to calculate, for example, the contribution of the transition zone (from a point $\zeta_i$ where the slope angle has an apparent value $\alpha$ to the points $\zeta_c$ where the slope angle is $\alpha_s$; see figure 5) to the normal force per unit contact-line length exerted on a plane, we obtain

$$\begin{aligned}\Delta F_n &= -\int_{\zeta_i}^{\zeta_c} f_n|_{\eta=0}\,\mathrm{d}\zeta \approx -\int_{\zeta_i}^{\zeta_c} f_n^0|_{\eta=0}\,\mathrm{d}\zeta + \int_{\zeta_i}^{\zeta_c}\sigma\frac{\mathrm{d}\sin\delta}{\mathrm{d}\zeta}\,\mathrm{d}\zeta \\ &= -\int_{\zeta_i}^{\zeta_c} f_n^0|_{\eta=0}\,\mathrm{d}\zeta + \sigma(\sin\alpha_s - \sin\alpha).\end{aligned} \tag{29}$$

Here, $f_n = \boldsymbol{f}\cdot\boldsymbol{n}$, and $\eta$ is the coordinate normal to the plane, with the plane corresponding to $\eta = 0$, whereas the plane is either the fibre, or the pad and substrate surface.

https://doi.org/10.1017/S0022112006004009 Published online by Cambridge University Press

Thus, the overall contribution to the force of the part of the plane from a point $\zeta$ outside the transition zone to the contact line is

$$F_n(\zeta) = -\int_{\zeta}^{\zeta_i} f_n|_{\eta=0}\,\mathrm{d}\zeta + \Delta F_n - \sigma\sin\alpha_s \approx -\int_{\zeta}^{\zeta_c} f_n^{(0)}|_{\eta=0}\,\mathrm{d}\zeta - \sigma\sin\alpha. \tag{30}$$

From (30), it can be seen that the force (and its moment) exerted on the plane is determined only by the non-singular part of the stress distribution $\boldsymbol{f}^0$ at the plane surface and the apparent contact angle $\alpha$ which may differ from $\alpha_s$. Then, if we want to calculate the forces exerted on the plane (the fibre, or the pad and substrate), we can avoid consideration of the vicinities of the contact lines $CL_1$, $CL_2$ and $CL_p$, even though they would move. The spreading velocities are very small in comparison with the macroscopic bulk velocities of the problem (Hoffman 1975; Dussan V. 1979), which seems to be true even in the case of reactive wetting/spreading. An order of magnitude estimate of the velocity of the contact line following from experiments is $0.2\,\mathrm{cm\,s^{-1}}$. For $\sigma = 480\,\mathrm{dyn\,cm^{-1}}$ and $\mu = 22\,\mathrm{g\,cm^{-1}\,s^{-1}}$ the estimate of the velocity of the contact line corresponds to $0.01\sigma/\mu$. The duration of the surface-tension-driven stage (ii) is about 30 ms and thus the contact lines can advance over the pad and the fibre only to a distance of about $6\times10^{-3}$ cm which is confirmed by the experimental movies and is negligibly small compared to the drop size of the order of $10^{-1}$ cm. (During the spreading stage (i) of a duration of about 3 s the advance of the contact lines is quite significant, 0.6 cm). Since a sufficiently strong macroscopic flow and the whole system shape are only slightly affected by the contact line motion, we shall use, for simplicity, the no-slip boundary conditions (8) and (9) at the contact lines, as though they were fixed. Actually, the stationary value of the contact angle $\alpha_s$ can be restored only at the very end, after the macroscopic bulk motion has faded. Note that it does not mean that the contact line motion does not play any role in the fibre alignment. The droplet shape elongated along the fibre and required for its alignment (see figure 4*b*) can result only from the spreading stage (i).

Note also that because the geometry of the surface near the contact lines $CL_1$ and $CL_2$ is complicated, we might not have a sufficient number of nodes per unit length on them (see figure 4*c*). As a result, significant errors in the line integrals along $CL_1$ and $CL_2$ in (25) and (26) can emerge. Therefore, it is much more convenient to calculate the values of $\boldsymbol{F}$ and $\boldsymbol{M}$ using the right-hand sides of the equations (25) and (26), because the geometrical configuration near the contact line $CL_p$ is much simpler (we also suppose that $CL_p$ does not move).

The initial conditions should be specified, determining the initial positions of the free surface and the fibre, as well as its angular velocity

$$\boldsymbol{r}_i(0) = \boldsymbol{r}_i^0, \quad \varphi(0) = \varphi^0, \quad \psi(0) = 0, \quad y_{cm}(0) = y_{cm}^0, \quad z_{cm}(0) = z_{cm}^0, \tag{31}$$

$$\omega(0) = \omega^0, \quad V_y(0) = V_y^0, \quad V_z(0) = V_z^0, \tag{32}$$

where $\boldsymbol{r}_i^0$ is the initial position vector ($t=0$) of the $i$th node at the free surface. We suppose $\omega^0 = 0$, $V_y^0 = 0$, $V_z^0 = 0$.

## 5. Numerical implementation

Equations (7), (11)–(18) can be solved numerically using the Kutta–Merson method, provided the values $\boldsymbol{u}(\boldsymbol{r}_i)$, $\boldsymbol{F}$ and $\boldsymbol{M}$ are known for any given moment of time. The latter are found from the Stokes equations (2) and (3) with the boundary conditions (4),(8) and (9). These equations are equivalent to a set of the following integral

https://doi.org/10.1017/S0022112006004009 Published online by Cambridge University Press

equations convenient for numerical integration (Becker 1992; Pozrikidis 1992)

$$c_{ij}(\boldsymbol{x}_0)u_i(\boldsymbol{x}_0) = \oint_\Gamma f_i(\boldsymbol{x})G_{ij}(\boldsymbol{x}, \boldsymbol{x}_0)\,\mathrm{d}S - \text{p.v.} \oint_\Gamma u_i(\boldsymbol{x})T_{ijk}(\boldsymbol{x}, \boldsymbol{x}_0)n_k(\boldsymbol{x})\,\mathrm{d}S, \qquad (33)$$

where the second integral is evaluated in the principal value sense. The kernels $G_{ij}$ and $T_{ijk}$ are the velocity and force parts of the three-dimensional Green's function in the free space

$$G_{ij}(\boldsymbol{x}, \boldsymbol{x}_0) = \frac{1}{8\pi\mu}\left(\frac{\delta_{ij}}{r} + \frac{\hat{x}_i\hat{x}_j}{r^3}\right), \quad T_{ijk}(\boldsymbol{x}, \boldsymbol{x}_0) = -\frac{3}{4\pi}\frac{\hat{x}_i\hat{x}_j\hat{x}_k}{r^5}, \qquad (34)$$

where $\hat{x}_i = x_i - x_{0i}$, $r = |\boldsymbol{x} - \boldsymbol{x}_0|$ (points $\boldsymbol{x}$ and $\boldsymbol{x}_0$ being located at the boundary of the liquid volume $\Gamma$), $c_{ij}$ is a matrix with elements depending on the corner angle of the boundary surface $\Gamma$ at point $\boldsymbol{x}_0$ (the boundary is not necessarily supposed to be a Lyapunov surface).

Equation (33) is solved using the boundary element method (BEM) described in detail in Becker (1992) and Pozrikidis (1992). To solve (33) numerically, we used a code based on BEACON of Becker (1992), originally developed for two-dimensional elastostatic problems and modified for the present low-Reynolds-number hydrodynamic three-dimensional problem. The quadrilaterial surface elements were used and then the bilinear approximation for the surface was used inside each element. The mean curvature $\kappa$ was calculated using the iterative method described in Zinchenko *et al.* (1997). In this method, the local approximation of the surface by the quadratic function was used in the vicinity of each node. This method yields good results for surfaces with transition regions where the mean curvature changes its sign (Zinchenko *et al.* 1997), which may indeed take place in the problem under consideration at some moments of time. The comparison of the results obtained by this method with the results obtained by another iterative method (Rallison 1984) yields the maximum relative error $\sim$5 % for the surfaces characteristic of the present problem. This is a good result for the sufficiently rough grids used here.

After the velocity at the free surface $\boldsymbol{u}$ and values of $\boldsymbol{F}$ and $\boldsymbol{M}$ are found from (33) and (4), (8), (9) at each time step, the system (7), (11)–(18) is integrated to follow the time evolution of the free surface and the fibre motion.

The initial shape of the liquid surface with the fibre inserted in the drop was built in the following manner. The straight contact lines $CD$ and $AE$ in figure 4($a$) corresponded to the drop spreading at the end of stage (i) in the experiment. Between the straight contact lines in figure 4($a$) a three-dimensional drop configuration with embedded fibre corresponding to the symmetric drop shape shown in figure 4($b$) (the fibre is parallel to the pad) and the grid on its surface were constructed using the software system for generating three-dimensional grids and meshes, GRIDGEN. The drop in figure 4($b$) is symmetric relative to planes $y = 0$ and $z = 0$ (cf. figure 4$a$). To construct more complicated initial shapes existing in the experiments (similar to the one shown in figure 4$c$), the symmetric mesh of figure 4($b$) obtained by GRIDGEN was used as an input for the code, where some constant values of $\omega_\varphi$, $V_y$, $V_z$ were set in the boundary condition (9), (10), (19) to introduce a uniform displacement and rotation of the fibre, which are kept virtually constant by some applied force and moment of force acting on the fibre (during this preparatory stage). Then, equations (7), (15)–(17), (33) were solved to determine the corresponding evolution of the drop surface up to the time when the desired deviations $\varphi^0$, $y^0_{cm}$ and $z^0_{cm}$ were obtained. Then the shape obtained (see, for example, figure 4$c$) was used as an initial condition for the problem under consideration.

https://doi.org/10.1017/S0022112006004009 Published online by Cambridge University Press

## 6. Dimensionless parameters

Introduce the following dimensionless variables

$$\boldsymbol{r}' = \frac{\boldsymbol{r}}{a_0}, \quad t' = \frac{t}{T_0}, \quad \omega' = T_0\omega, \quad \boldsymbol{u}' = \frac{\boldsymbol{u}}{V_0}, \quad p' = \frac{a_0 p}{\sigma}, \quad \kappa' = \kappa a_0, \tag{35}$$

where the length scale $a_0$ is the radius of a hemisphere that contained the same volume as the drop, the velocity scale $V_0 = \sigma/\mu$ and the time scale $T_0 = \mu a_0/\sigma$.

The dimensionless dynamic boundary condition at the free surface (4) takes the form

$$\boldsymbol{f} = \kappa \boldsymbol{n}, \tag{36}$$

Here and hereinafter, the primes over the dimensionless parameters are dropped for brevity. The equations of the fibre motion take the form

$$\frac{\mathrm{d}\boldsymbol{u}_{cm}}{\mathrm{d}t} = \widetilde{\beta}\boldsymbol{F}, \tag{37}$$

$$I_1\frac{\mathrm{d}\omega_\varphi}{\mathrm{d}t} = \widetilde{\beta}M_x, \tag{38}$$

$$I_2\frac{\mathrm{d}\omega_\psi}{\mathrm{d}t} = \widetilde{\beta}(M_y\cos\varphi + M_z\sin\varphi), \tag{39}$$

where

$$\boldsymbol{F} = \int_{pad+substrate} \boldsymbol{f}\, dS + \oint_{CL_p} \boldsymbol{t}\,\mathrm{d}l, \tag{40}$$

$$\boldsymbol{M} = \int_{pad+substrate} \widetilde{\boldsymbol{r}} \times \boldsymbol{f}\,\mathrm{d}S + \oint_{CL_p} \widetilde{\boldsymbol{r}} \times \boldsymbol{t}\,\mathrm{d}l, \tag{41}$$

$$I_1 = \frac{I_x}{ma_0^2}, \tag{42}$$

$$I_2 = \frac{I_0}{ma_0^2}. \tag{43}$$

The parameter $I_1$ denotes the dimensionless moment of inertia of a cylindrical fibre relative to the $x$-axis. In the present case, $R_0 \ll l_0$, and then

$$I_x \simeq \frac{ml_0^2}{3}, \quad I_1 \simeq \frac{1}{3}\left(\frac{l_0}{a_0}\right)^2. \tag{44}$$

The parameter $I_2$ denotes the dimensionless moment of inertia of a cylindrical fibre relative to its own axis

$$I_0 = \frac{mR_0^2}{2}, \quad I_2 = \frac{1}{2}\left(\frac{R_0}{a_0}\right)^2. \tag{45}$$

Also

$$\widetilde{\beta} = \frac{\mu V_0 a_0^2}{mV_0^2} = \frac{\mu^2 a_0^2}{m\sigma}, \tag{46}$$

characterizes the ratio between the viscous dissipative losses and the characteristic kinetic energy of the fibre.

https://doi.org/10.1017/S0022112006004009 Published online by Cambridge University Press

In the following, we shall consider two force (moment) components $\boldsymbol{F}_1$ ($\boldsymbol{M}_1$) and $\boldsymbol{F}_2$ ($\boldsymbol{M}_2$)

$$\boldsymbol{F}_1 = -\int_{fibre} \boldsymbol{f}\,\mathrm{d}S, \quad \boldsymbol{F}_2 = -\oint_{CL_1} \boldsymbol{t}\,\mathrm{d}l - \oint_{CL_2} \boldsymbol{t}\,\mathrm{d}l = \boldsymbol{F} - \boldsymbol{F}_1, \tag{47}$$

$$\boldsymbol{M}_1 = -\int_{fibre} \boldsymbol{r} \times \boldsymbol{f}\,\mathrm{d}S, \quad \boldsymbol{M}_2 = -\oint_{CL_1} \widetilde{\boldsymbol{r}} \times \boldsymbol{t}\,\mathrm{d}l - \oint_{CL_2} \widetilde{\boldsymbol{r}} \times \boldsymbol{t}\,\mathrm{d}l = \boldsymbol{M} - \boldsymbol{M}_1, \tag{48}$$

where $\boldsymbol{F}_1$ ($\boldsymbol{M}_1$) is the force (moment) related to the viscous stresses acting on the fibre surface located inside the drop, and $\boldsymbol{F}_2$ ($\boldsymbol{M}_2$) is related to the capillary forces exerted at the contact lines $CL_1$ and $CL_2$ (as in Powell, Warren & Bailey 1998).

Equations (33) and (34) do not change on being recast into the dimensionless form except that $\mu$ is replaced by 1. Equations (15)–(18) also do not change after being written in dimensionless form.

## 7. Numerical simulations for three-dimensions: results and discussion

At first, we consider the angular motion of the fibre about the $x$-axis, passing through its motionless centre-of-mass. This type of motion is realized when the initial surface shape corresponds to the symmetrical initial conditions

$$x(y, z) = x(-y, -z), \quad y_{cm} = z_{cm} = 0 \text{ at } t = 0. \tag{49}$$

In this case, $F_y = F_z = M_y = M_z = 0$ and the centre-of-mass is motionless. Then conditions (49) will be conserved for all the subsequent drop evolution, and the fibre will not rotate around its own axis. The fibre motion is described by only the $x$-projection of the moment-of-momentum balance, namely (38). We can rewrite this equation as

$$\frac{\mathrm{d}\omega_\varphi}{\mathrm{d}t} = 3\beta M_x, \tag{50}$$

where

$$\beta = \frac{\mu^2 a_0^4}{m\sigma l_0^2} \tag{51}$$

is the dimensionless parameter including the physical properties of the liquid and the main geometrical scales of the drop and fibre. Another important geometrical parameter involved is the half-length of the pad $a$ rendered dimensionless by $a_0$ (see figure 1).

The initial angle between the fibre and the pad centrelines in the calculations was $\varphi^0 = 0.3$ (about 17.2°). The evolution of the free surface of the liquid was found numerically for the different values of $a/a_0$ and $\beta$. An example for $a/a_0 = 1.3$ is shown in figure 6. The time dependences of the angle between the fibre and the pad centrelines $\varphi(t)$ for the different values of $\beta$ are shown in figure 7. From this figure, it can be seen clearly that the angle $\varphi$ tends to zero as $t \to \infty$ in all the cases. This means that the drop reorients the fibre parallel to the pad centreline (the alignment effect). The characteristic time of the process is very large for $a/a_0 = 1.1$ when the initial drop shape is close to the spherical one and decreases as the value of the ratio $a/a_0$ increases. If we determine the characteristic time $T_e$ of the fibre evolution as the dimensionless time when $\varphi(T_e) = \varphi^0/3$, then $T_e \simeq 5$ for $a/a_0 = 1.3$ and $T_e \simeq 2$ for $a/a_0 = 1.5$.

As can be seen from figure 7, all the curves for various values of $\beta$ behave rather similarly as $t$ increases (for $\beta = 0.25$ and 1, fibre inertia is still important; for $\beta = 5$, it

https://doi.org/10.1017/S0022112006004009 Published online by Cambridge University Press

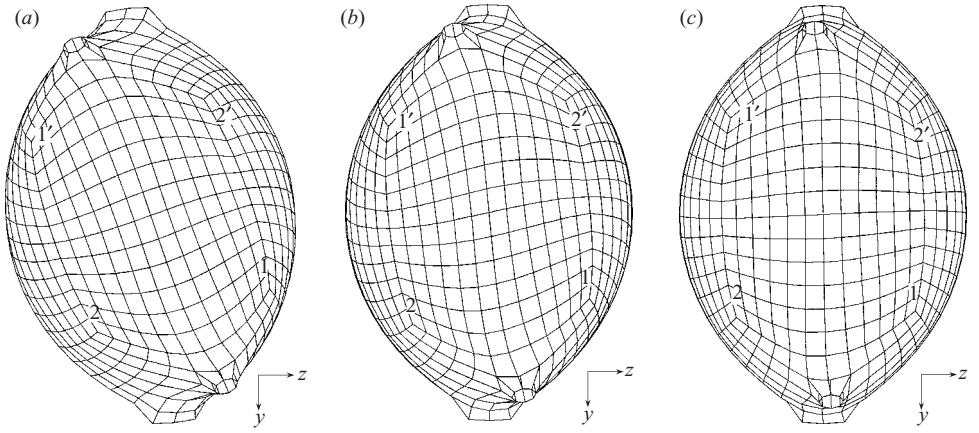



FIGURE 6. Evolution of the fibre–solder system found numerically for $a/a_0 = 1.3$, $\beta = 0.25$, $R_0/a_0 = 0.075$, $x_{cm}/a_0 = 0.5$. (*a*) $t = 0$, (*b*) $t = 2$, (*c*) $t = 11.45$.

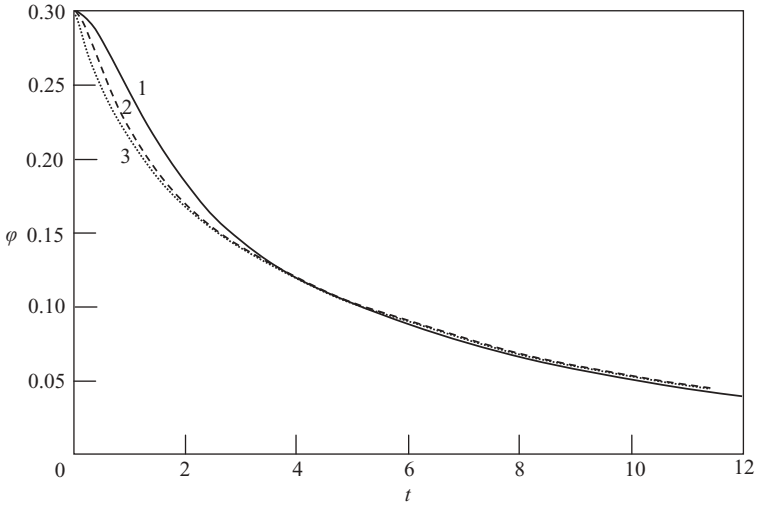



FIGURE 7. Evolution of the angle between the fibre and the pad centrelines. $a/a_0 = 1.3$. Curve 1 corresponds to $\beta = 0.25$; 2, $\beta = 1$; 3, $\beta = 5$.

can already be neglected). Even in the case of $\beta = 0.25$, the fibre inertia plays a role only at the initial stage of the fibre evolution. The numerical calculations show that the asymptotic form of the dependence $\varphi(t)$ at small values of $\varphi$ is

$$\varphi \sim \exp(-\lambda t), t \to \infty, \tag{52}$$

where the decrement $\lambda(a/a_0, t)$ depends on $t$ only slightly; probably it also depends on the fibre radius $R_0$, but the present simulations do not allow us to quantify the dependence; however, $\lambda$ strongly depends on the ratio $a/a_0$. For example, for $a/a_0 = 1.3$ we found $\lambda \approx 0.12$, and for $a/a_0 = 1.5$ it was $\lambda \approx 0.19$. Note that (52) suggests that at small values of $\varphi$ the moment of forces related to surface tension acting on the fibre is $\sim \sigma a_0^2 \varphi$, which in the inertialess cases is balanced by the moment of viscous forces $\sim \mu(\mathrm{d}\varphi/\mathrm{d}t)2\pi R_0 a_0^2$.

https://doi.org/10.1017/S0022112006004009 Published online by Cambridge University Press

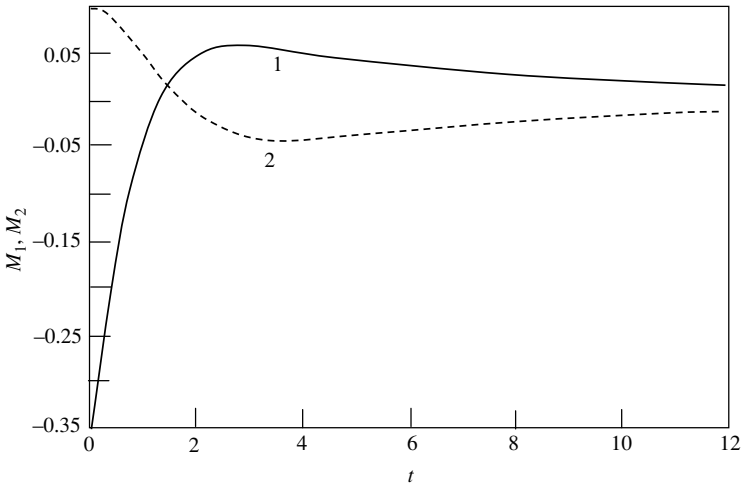



FIGURE 8. Evolution of the components of the moment of the forces acting at the fibre surface and at the contact lines for $a/a_0 = 1.3$, $\beta = 0.25$. Curve 1 corresponds to $M_1$; curve 2, to $M_2$.

The question of which component of the moment of forces plays the main role in the alignment process arises. The time dependences of the components of the moment $M_{1x}$ and $M_{2x}$ (cf. (48)) for $a/a_0 = 1.3$ are presented in figure 8 (the subscript $x$ will be dropped for brevity in the following). From this figure, we see that for the initial drop shape assumed, the component $M_1 < 0$ stabilizes the fibre at the initial stage of the process. It can be explained by the following reasons. As can be seen from figure 6($a$), the absolute value of the mean curvature $\kappa$ at the location 1 (1′) on the surface is larger than that at the location 2 (2′) for the initial condition used. Then the pressure forces acting on the corresponding sides of the fibre from the drop are different. Accordingly, a stabilizing moment of the capillary pressure sets in at $t = 0$, pulling the fibre back toward the pad centreline. Thus, the stabilizing effect at the initial stage of the process is provided mostly by the first component of the moment, $M_1 < 0$. After the initial stage of the process, the second component, $M_2 < 0$, begins to play the main role in the fibre alignment (see figure 8), while the component $M_1$ becomes positive owing to the action of the viscous dissipative forces. The approximate equality $M_2 \simeq -M_1$ is realized for $t \geqslant 1$ (see figure 8).

The three-dimensional calculations were also conducted for more complicated initial conditions, when the centre-of-mass of the fibre has been displaced from the point $(x_{cm}, 0, 0)$ by the method described at the end of § 4 (see figure 4$c$). The initial fibre position corresponded to the following initial values of the centre-of-mass coordinates and the angle between the fibre and the pad centreline

$$y_{cm}^0 = z_{cm}^0 = 0.2, \quad \varphi^0 = 0.3 \ (17.2^\circ). \tag{53}$$

The system of equations (11)–(18) was solved to find the evolution of the fibre-solder system for the case of $\widetilde{\beta} = 1$. The corresponding time dependences for $y_{cm}(t)$, $z_{cm}(t)$, $\varphi(t)$ and $\psi(t)$ are shown in figure 9. From this figure, we see that the curves $y_{cm}(t)$, $z_{cm}(t)$, $\varphi(t)$ tend to zero, which means that the fibre returns to the centred position over the pad. As can be seen from figure 9, the characteristic time of relaxation of the initial displacement of the centre-of-mass is much shorter than that for the angular alignment.

https://doi.org/10.1017/S0022112006004009 Published online by Cambridge University Press

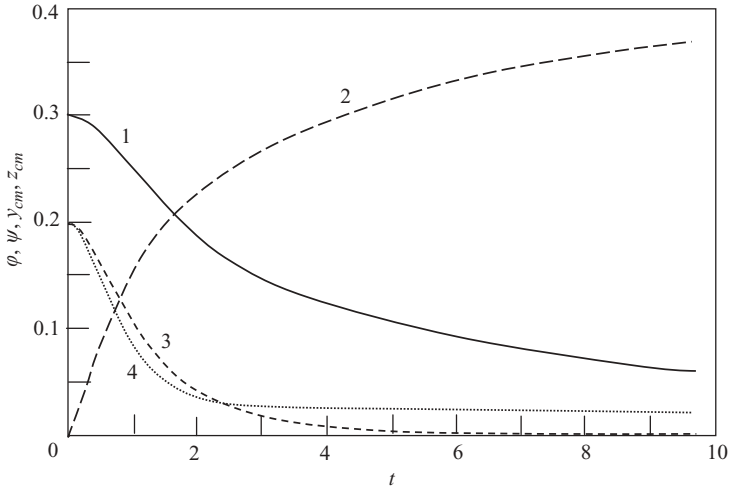



FIGURE 9. Evolution of the coordinates of the centre-of-mass of the fibre and the angles determining the position of the fibre for the parameters $a/a_0 = 1.3$, $\widetilde{\beta} = 1$. Curve 1 corresponds to the dependence $\varphi(t)$; 2, to $\psi(t)$; 3, to $y_{cm}(t)$; 4, to $z_{cm}(t)$.

Three-dimensional numerical calculations have also been conducted for the case where the fibre is not horizontal and can be initially inclined over the pad by an angle $\theta$. The fibre is assumed to be sufficiently short not to touch the pad at $t = 0$. The equations for $\theta$ in the dimensionless variables (35) are

$$\frac{\mathrm{d}\omega_\theta}{\mathrm{d}t} = 3\beta M_z, \tag{54}$$

$$\frac{\mathrm{d}\theta}{\mathrm{d}t} = \omega_\theta. \tag{55}$$

(the fibre centre-of-mass is supposed to be fixed inside the drop). The drop–fibre evolution is shown in figure 10. The angle $\theta$ between the fibre and the pad plane tends to zero. This means that the alignment process takes place in this case also, and the fibre tends to become parallel to the pad. Numerical calculations show that the asymptotic law of the time dependence $\theta(t)$ is exponential and similar to that in (52).

The experiments showed that the alignment process takes place for any initial conditions. For example, we can set the initial condition in the following manner: rotate the fibre from the position shown in figure 4(*b*) to some angle $\varphi$ and then hold it up to the time moment when the liquid motion is stopped owing to viscous dissipation. In that case, the mean curvature tends to a constant value $\kappa_0$, the pressure – to $\sigma\kappa_0$ and then $M_1 = 0$ if the contact lines do not change their position. Numerical calculations show that also in this case $M_2 < 0$, and the drop aligns the fibre near the pad centreline.

The three-dimensional calculations are involved and one is tempted to ask whether a simplified two-dimensional model can capture some important features. Such a model is presented in the Appendix. It mimics, indeed, some of the three-dimensional phenomena (in particular, fibre alignment due to surface tension in the drop), but some not all. For example, the two-dimensional model does not allow the plate (the two-dimensional fibre) to pass over the pad, whereas in the three-dimensional case the fibre, in principle, can pass over the pad. Also, the two-dimensional model allows

https://doi.org/10.1017/S0022112006004009 Published online by Cambridge University Press

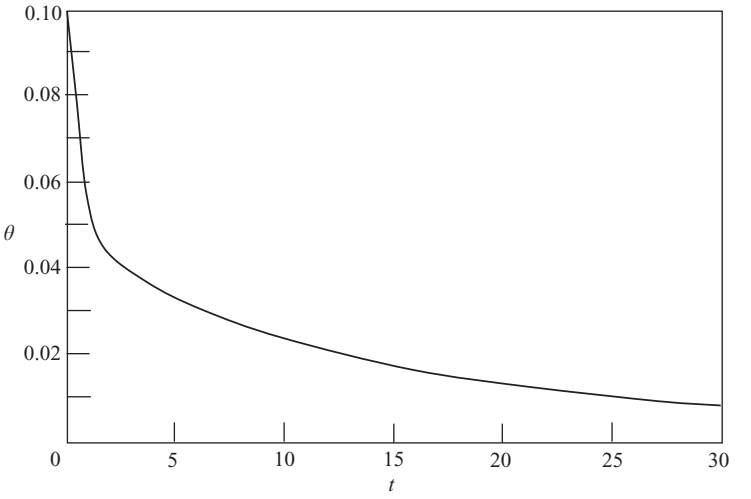



FIGURE 10. Evolution of the angle between the fibre and the pad plane $\theta(t)$. The parameters are: $a/a_0 = 1.3$, $R_0/a_0 = 0.075$, $\widetilde{\beta} = 1$, the initial angle of rotation $\theta^0 = 0.1(5.73\,^\circ)$.

static configurations shown in figure 16(*b*) (since it, in fact, corresponds to two drops separated by the plate), whereas in the three-dimensional case they are impossible. Therefore, in the real situation the three-dimensionality of the problem is the key element for the fibre alignment.

## 8. Comparison of the predictions with the experimental data and additional discussion

The results of the numerical simulations for the surface-tension-driven stage (ii) were compared to the experimental data. The dependence of viscosity on temperature is unknown in detail, but widely believed to be Arrhenius-like. Therefore, the uncertainties in the temperature values in the experiment can significantly affect the solder viscosity. The uncertainties in temperature might be due to the inaccuracies related to the thermal capacity of the thermocouple used for the average temperature control, temperature feedback system used, differences in droplet positioning relative to the heat source, etc. In particular, a special source of inaccuracy is due to the temperature measurement technique. The solder droplet (millimetre scale) is located on a substrate (silicon wafer coated with several metal layers) which is mounted on a heat source. Temperature measurements rely on a thermocouple which is attached to the silicon wafer in the vicinity of the droplet. Therefore, we should expect some inaccuracy in the observed temperature of the droplet. More than that, because disturbances (ambient temperature, motion of the optical fibre) are faster than the controller dynamics, we can only guarantee that the temperature at the measurement point is close ($\pm 2\,^\circ$C) to the required temperature rather than equal to the set point. These reasons can be sufficient to result in temperature variation of the order of $1\,^\circ$C (or even several degrees), and, via the Arrhenius law, in a significant viscosity variation. There are several additional reasons that can affect viscosity values. As mentioned in § 3, we are dealing with the so-called 'reactive spreading' when pad metals dissolve in the solder droplet and various intermetallics are formed (e.g. copper/tin, gold/tin). It is well known that even the slightest traces of intermetallics can lead to dramatic changes in physical properties of liquid metals, and especially of such alloys as solder. Examples

https://doi.org/10.1017/S0022112006004009 Published online by Cambridge University Press

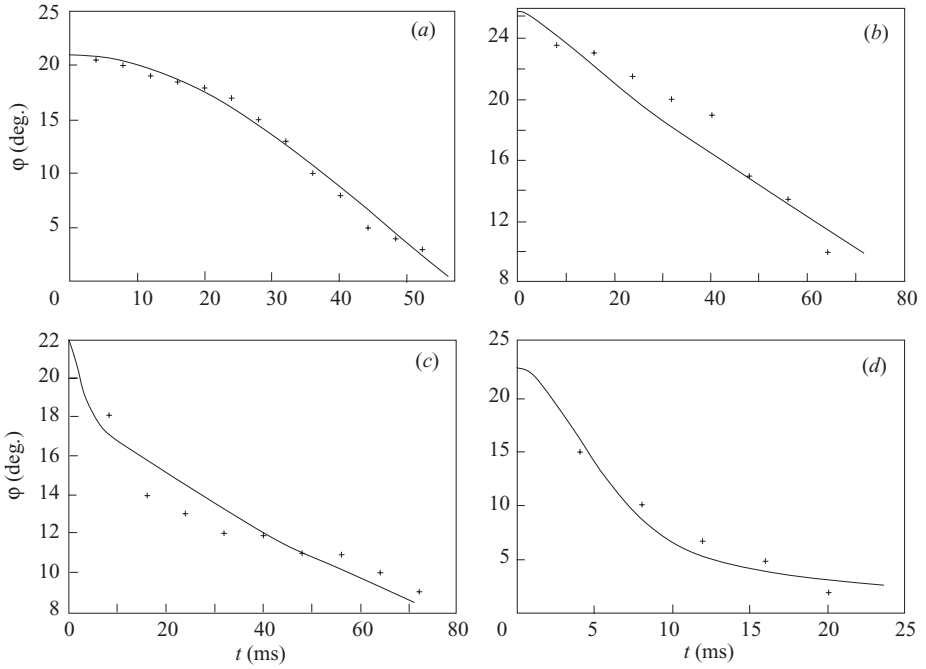



FIGURE 11. Measured and predicted evolution of the angle $\varphi$ between the fibre and the pad centrelines. The parameters used in the three-dimensional numerical calculations were the following: (*a*) the dimensionless pad length $a/a_0 = 1.5$, $\beta = 0.001$ (with $\mu = 12.2\,\mathrm{g\,cm^{-1}\,s^{-1}}$, $\sigma = 480\,\mathrm{g\,s^{-2}}$), the fibre half-length $l_0 = 2.4\,\mathrm{cm}$, the drop volume $1.2 \times 10^{-3}\,\mathrm{cm^3}$; (*b*) $a/a_0 = 1.1$, $\beta = 0.012$ (with $\mu = 8.64\,\mathrm{g\,cm^{-1}\,s^{-1}}$, $\sigma = 480\,\mathrm{g\,s^{-2}}$), the fibre half-length $l_0 = 0.8\,\mathrm{cm}$, the drop volume $1.2 \times 10^{-3}\,\mathrm{cm^3}$; (*c*) $a/a_0 = 1.1$, $\beta = 0.25$ (with $\mu = 10.9\,\mathrm{g\,cm^{-1}\,s^{-1}}$, $\sigma = 480\,\mathrm{g\,s^{-2}}$), the fibre half-length $l_0 = 0.35\,\mathrm{cm}$, the drop volume $1.2 \times 10^{-3}\,\mathrm{cm^3}$; (*d*) $a/a_0 = 1.5$, $\beta = 0.25$ (with $\mu = 30.2\,\mathrm{g\,cm^{-1}\,s^{-1}}$, $\sigma = 480\,\mathrm{g\,s^{-2}}$), the fibre half-length $l_0 = 0.5\,\mathrm{cm}$, the drop volume $0.67 \times 10^{-3}\,\mathrm{cm^3}$. Curves correspond to the results of the numerical calculations; symbols, experimental data. The error bars corresponding to the experimental data are of the order of $1^\circ$ at the beginning of stage (ii) and about $2^\circ$ close to its end. In all the cases, most of the fibre protruded from the drop.

of this kind were given in our previous publications on liquid gallium and on a similar solder/metallization system (Priede *et al.* 1999; Salalha *et al.* 2004). Therefore, viscosity values in our present case might also be affected not only by temperature variation, but by intermetallics formed in the droplet owing to dissolution of pad metals. The above reasons explain why despite wide applications of solder, it is impossible to find complete thermophysical data. Also, viscosity measurements for a material at about 200°C represent a complicated experimental problem. Under such circumstances, the best phenomenological and pragmatic way to characterize the liquid is to fit to the actual data in the representative cases. Therefore, viscosity was slightly fitted to find an appropriate time scale $T_0$ from (35). The viscosity values found are given in the caption to figure 11. Comparison of the viscosity values corresponding to figures 11(*a*), 11(*b*) and 11(*c*) shows that they correspond to approximately the same thermal situation. As the sensitivity analysis shows, the data can be equally described using any of the viscosity values in the range 8.64 to $12.2\,\mathrm{g\,cm^{-1}\,s^{-1}}$. On the other hand, temperature was significantly lower in the experiment corresponding to figure 11(*d*) and as a result, the viscosity value there is significantly higher than those in the cases of figures 11(*a*)–11(*c*). For comparison with the experiments, the three-dimensional calculations were

https://doi.org/10.1017/S0022112006004009 Published online by Cambridge University Press

conducted. The predicted evolution of the angle $\varphi$ between the fibre and the pad centrelines is shown in figure 11 versus the experimental data. The agreement between the data and the predictions is reasonable. The differences between the numerical and the experimental curves in figure 11 may be related to the inertial effects. Indeed, in the experiment, because of the temperature uncertainties, the Reynolds number *Re* can be of the order of 1, and some traces of the fibre tendency to begin to oscillate are visible in the experimental data in figure 11. Also the friction forces between the fibre and the pad, not accounted for in the numerical simulations, can play some role at longer times. Figure 11 shows that the predicted duration of the surface-tension-driven alignment is of the order of $10^2$ ms which corresponds to the experimental results. The duration depends on the value of the initial drop stretching along the pad, $a/a_0$, related to wettability and, in fact, determined by the pad length. For example, for figures 11(*c*) and 11(*d*), $a/a_0 = 1.1$ and 1.5, respectively, whereas the value of $\beta = 0.25$ is the same. Therefore, the increase of $a/a_0$ from 1.1 to 1.5 at a fixed $\beta = 0.25$ yields a decrease of the duration of the alignment process from about 60 ms to about 20 ms, respectively.

Note that in the cases when $\beta \ll 1$, i.e. the fibre inertia is significant, the angle $\varphi$ can 'undershoot' and become negative before approaching zero, as for example, would happen for $\beta = 0.001$ of figure 11(*a*) at larger values of $t$. In this case, the asymptotic behaviour described by (52) could not be realized. Also, the numerical calculations show that an 'undershoot' would happen with $\beta = 0.01$ and $a/a_0 = 1.3$ for $t > 16$ (dimensionless). On the other hand, in figures 11(*b*)–(*d*) corresponding to $\beta = 0.012$, 0.25 and 0.25, respectively, the asymptotic behaviour corresponding to (52) does occur at higher values of $t$ (in figures 11*b* and 11*c* the frame begins from 8°). The experimental data, however, do not extend that far.

## 9. Conclusion

It has been shown that the process of fibre self-assembly in a solder drop consists of two distinct stages. At the initial, relatively long stage (i), which lasts several seconds, a solder drop melts and spreads over the pad and the fibre, which results in a slight reorientation of the fibre. At stage (ii), the surface tension diminishes the surface area of the solder drop. This stage is relatively short and results in an almost perfect fibre orientation along the pad centreline.

For the surface-tension-driven stage (ii), the three-dimensional direct numerical simulations of the present work showed that for the fibres strictly parallel to the pad plane there are two equilibrium states: (*a*)$\varphi = \pi/2$ (the fibre is normal to the pad centreline), which is, obviously, unstable; and (*b*)$\varphi = 0$ (the fibre is aligned along the pad centreline), which is stable.

It was shown that when the fibre inertia is sufficiently small, the angle between the fibre and the pad centreline decreases exponentially, as $\varphi \sim \exp(-\lambda t)$ at sufficiently large $t$ when $\varphi$ is small. The decrement $\lambda$ depends on the initial spreading length of the drop along the pad. A simplified two-dimensional model is also proposed which mimics some important (but not all) features of the three-dimensional case. Moreover, the results for the two-dimensional model show that an optimal wetted pad length exists for which the alignment process at stage (ii) is the shortest.

The numerical three-dimensional calculations also showed that the initial displacement of the fibre centre-of-mass relative to the drop centre, as well as the fibre inclination angle $\theta$ in the vertical plane relative to the pad plane vanish under the action of surface tension, the former much faster then the latter. The dependence of the angle $\theta$ on time at sufficiently large $t$ follows an exponential trend similar to that of $\varphi$.

https://doi.org/10.1017/S0022112006004009 Published online by Cambridge University Press

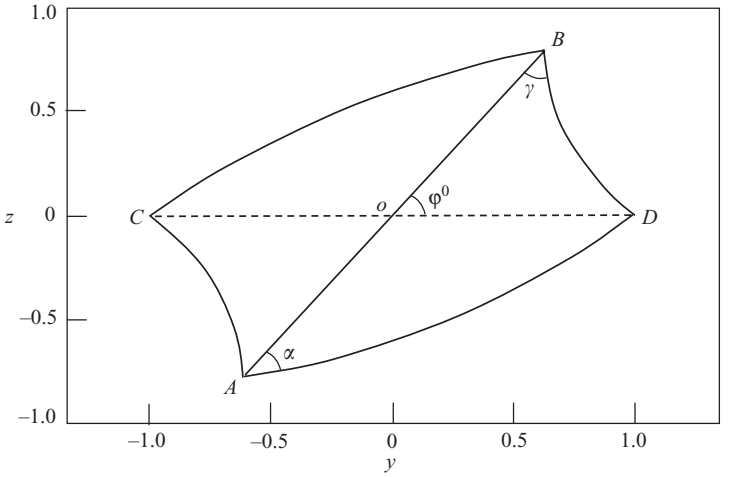



FIGURE 12. The initial configuration for the two-dimensional problem (top view). The plate $AB$ is submerged into the drop. The drop surface is pinned to the plate at $A$ and $B$, as well as it is pinned at the pad edges $C$ and $D$.

In addition, comparison of the numerical predictions to the experimental data revealed that the predicted characteristic time of the surface-tension-driven alignment process of the order of several tens of ms agrees with the duration of the fast stage (ii) recorded in the experiments.

## Appendix

A simplified two-dimensional model corresponding to the three-dimensional model of §§4–7 is readily available and tempting. The geometry of this model is shown in figure 12. The plate $AB$ of height $L_p$ in the $x$-direction (normal to the figure plane) and length $2l_0$ plays the role of the fibre in this model. The drop surface is pinned at the plate at $A$ and $B$, as well as at the pad at $C$ and $D$. The distances $AB$ and $CD$ were taken as equal for simplicity: $AB = CD = 2a$ (in this case it was $a_0 = a$). The initial shape of the liquid surface was taken as two circular arcs $AD$ and $DB$ with equal contact angles at the contact lines $A$ and $B$, $\alpha = \gamma = 0.7$ (40.1°) and $\varphi^0 = 0.9$ (51.57°). The arcs $AC$ and $CB$ are antisymmetric to $DB$ and $AD$.

Using the dimensionless variables described in §6, we obtain for this model

$$\beta = \frac{\mu^2 L_p a_0^3}{m\sigma l_0^2}. \tag{A 1}$$

The dimensionless components of the moment of the forces acting on the plate $AB$ read

$$M_1 = -2\int_{AB} f_n s \, \mathrm{d}s, \tag{A 2}$$

$$M_2 = 2a(\sin\alpha - \sin\gamma), \tag{A 3}$$

where $f_n$ is the component of the stress normal to the plate, $s$ is a coordinate of a point along the plate reckoned from its centre, $\alpha$ and $\gamma$ are the current contact angles at the contact lines $A$ and $B$. The deficiency of this model is that the plate cannot pass over the pad $CD$, even though the plate has inertia in the model. This results

https://doi.org/10.1017/S0022112006004009 Published online by Cambridge University Press

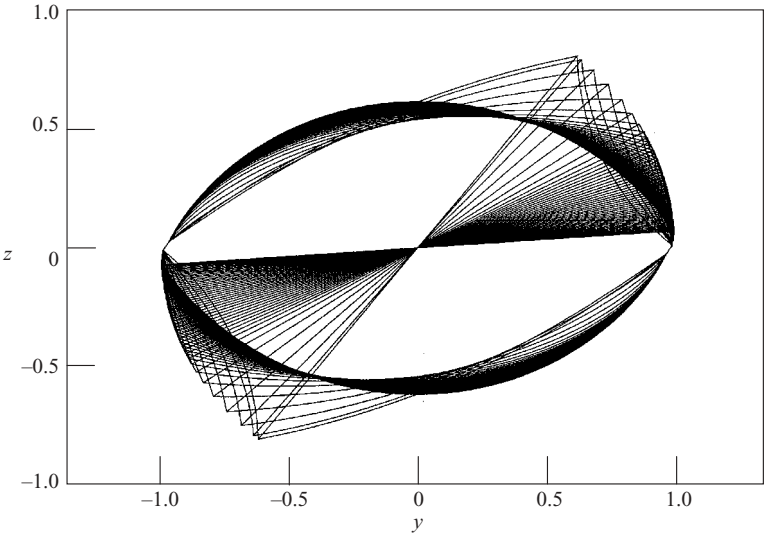



FIGURE 13. Evolution of the drop surface and the corresponding plate motion found numerically for $\beta = 1$ (two-dimensional problem). The time interval between the curves is $\Delta t = 0.2$. The initial contact angles were set as $\alpha = \gamma = 0.7$ (40.1°).

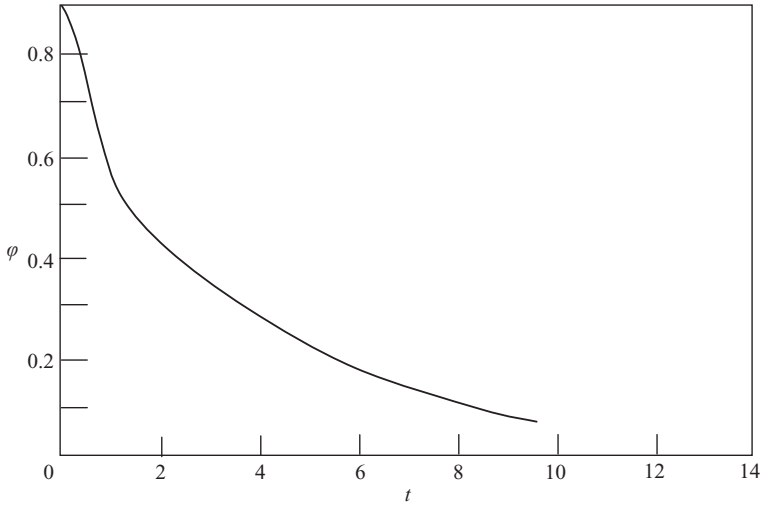



FIGURE 14. Evolution of the angle between the plate $AB$ and the pad $CD$ (two-dimensional problem). The initial angle $\varphi^0 = 0.9$, $\beta = 1$.

from the assumption that fluid velocity is zero at $C$ and $D$. In the three-dimensional case, an inertial fibre can, in principle, pass over the pad, albeit such cases have been found in the numerical calculations only for $\beta \leqslant 0.01$.

The flow in the two-dimensional drop is calculated using the two-dimensional counterpart of the three-dimensional equations (33) and (34). The plate motion is described using (50) with $M_x = M_1 + M_2$. An example of the time evolution of the plate and liquid surface for the case $\beta = 1$ is shown in figure 13. The time dependences of the angle $\varphi$ between the plate $AB$ and the pad $CD$ are shown in figure 14. The dependences $M_1(t)$ and $M_2(t)$ are shown in figure 15. From these figures, we see that

https://doi.org/10.1017/S0022112006004009 Published online by Cambridge University Press

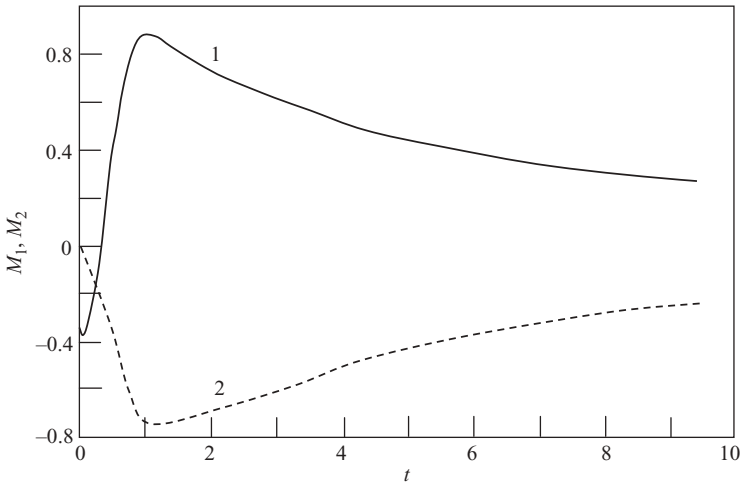



FIGURE 15. Evolution of the components of the moment of the forces acting at the plate surface, $M_1$, and at the contact lines, $M_2$ (two-dimensional problem). Curve 1 corresponds to $M_1$; 2, to $M_2$. $\beta = 1$.

initially the component $M_1$ pulls the plate to the pad $CD$ and a part of the surfaces $DB$ and $AC$ becomes convex. The value of $M_1$ changes its sign and cannot stabilize the plate near the pad $CD$; from the geometry for this type of surface, the inequality $\gamma > \alpha$ takes place (cf. figure 13), and most of the time the moment-of-force component $M_2 < 0$ is stabilizing. The dependences $\varphi(t)$ for $\beta = 1$ and $\beta = 10$ practically coincide for $t \geqslant 1$ (see figure 14). Note that the approximate equality $M_2 \simeq -M_1$ is realized for $t \geqslant 1$ (see figure 15) for the two-dimensional model as it was in the three-dimensional case. (However, that $M_2 < 0$ in the three-dimensional case is not as obvious as in the two-dimensional one.) Therefore, the simplified two-dimensional model in its main features is similar to the original three-dimensional model, and can be used for a qualitative explanation of the three-dimensional numerical results. For this aim and for the estimate of the characteristic time of the fibre alignment process, consider the balance of the moments of the forces acting on the plate, still given by (50) with $M_x = M_1 + M_2$. Similarly to the original three-dimensional model, we denote by $a_0$ the radius of the area-equivalent circle of a two-dimensional drop. After a while, the drop shape should become close to the equilibrium one – the shape symmetric relative to the pad $CD$ (see figure 16*a*). This equilibrium shape contains two circular arcs of equal radii

$$R = \frac{a}{\sin\alpha_0}, \tag{A 4}$$

with $CD = 2a$, where $a$ and $R$ are rendered dimensionless by $a_0$, $\alpha_0$ is the angle between the line $CD$ and the tangents to the arcs at points $C$ and $D$ (see figure 16*a*). The dimensionless relation between $a$ and $\alpha_0$ can be found from the condition of the area conservation

$$S = R^2(2\alpha_0 - \sin(2\alpha_0)) = \pi. \tag{A 5}$$

From (A 4) and (A 5), we find

$$a = \sqrt{\pi}\frac{\sin\alpha_0}{\sqrt{(2\alpha_0 - \sin(2\alpha_0))}}. \tag{A 6}$$

https://doi.org/10.1017/S0022112006004009 Published online by Cambridge University Press

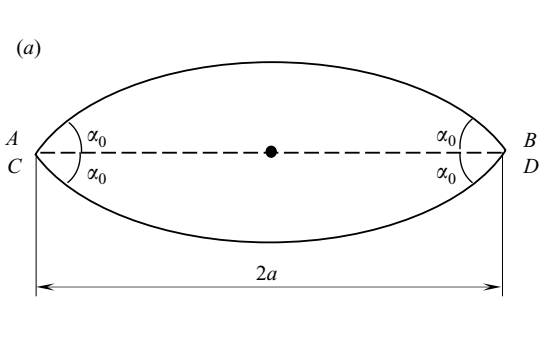



FIGURE 16. (*a*) Sketch of a symmetric static shape of a two-dimensional drop with the plate $AB$ aligned along the pad $CD$ ($\varphi = 0$). (*b*) The two-dimensional static configuration corresponding to the static contact angles achieved at all the contact lines before the moment when the plate $AB$ is released.

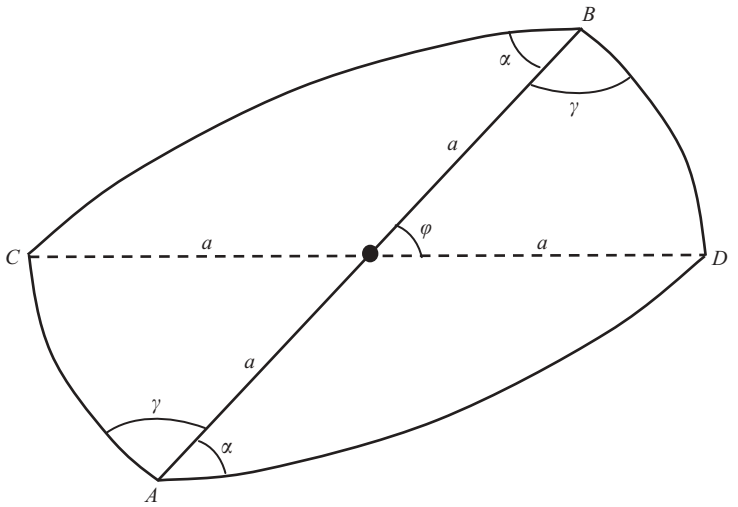



FIGURE 17. Sketch of the static shape of a two-dimensional drop with plate $AB$ not coinciding with line $CD$ ($\varphi > 0$).

Suppose that near the equilibrium, the motion is quasi-stationary and that the surface shape for small $\varphi > 0$ is close to the static one with the same $\varphi$ (i.e. the shape which would be realized in the case when someone holds the plate at this position) and the contact lines do not move relative to the plate and the pad. The stationary surface shape contains four arcs of equal radii

$$r = \frac{a\cos\varphi}{\sin\left(\alpha - \frac{1}{2}\varphi\right)} = \frac{a\sin\varphi}{\cos\left(\gamma - \frac{1}{2}\pi + \frac{1}{2}\varphi\right)}, \tag{A 7}$$

where $\alpha$ and $\gamma$ are the apparent contact angles at points $A$ and $B$ (see figure 17). The condition of the area conservation reads

$$S = 2r^2\left(\alpha + \gamma - \tfrac{1}{2}\pi - \tfrac{1}{2}\sin(2\alpha - \varphi) + \tfrac{1}{2}\sin(2\gamma + \varphi)\right) + 2a^2\sin\varphi = \pi. \tag{A 8}$$

https://doi.org/10.1017/S0022112006004009 Published online by Cambridge University Press

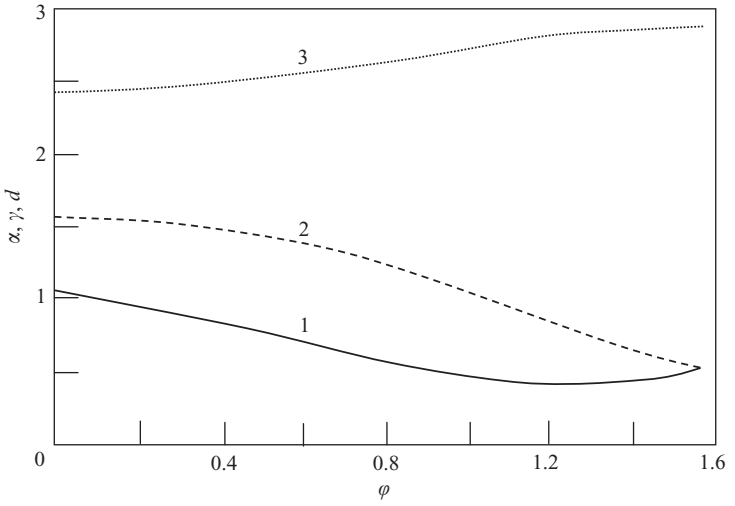



FIGURE 18. Dependences of the perimeter $d$ of the drop surface and the contact angles $\alpha$ and $\gamma$ at points $A$ and $B$ on the angle $\varphi$ between the plate $AB$ and the pad $CD$ for the shape shown in figure 17. The parameter $\alpha_0 = \pi/3$. Curve 1 corresponds to $\alpha(\varphi)$; 2, to $\gamma(\varphi)$; 3, to $d(\varphi)$.

From (A 7) and (A 8), we can find the dependences $\alpha(\varphi)$, $\gamma(\varphi)$ for a fixed value of $a$. The dimensionless surface energy $E_\sigma = d$, where $d$ is the perimeter of the drop surface

$$d = 4r\left(\alpha + \gamma - \tfrac{1}{2}\pi\right). \tag{A 9}$$

The dependences $\alpha(\varphi)$, $\gamma(\varphi)$, $d(\varphi)$ found from (A 7)–(A 9) for the case $\alpha_0 = \pi/3$ are shown in figure 18. From this figure we see that the drop perimeter $d$ and thus the surface energy $E_\sigma = d$, has a minimum at $\varphi = 0$. The stabilizing moment $M_2$ resulting from the surface tension forces is (cf. (A 3))

$$M_2 = -\frac{\mathrm{d}E_\sigma}{\mathrm{d}\varphi} = 2a[\sin(\alpha(\varphi)) - \sin(\gamma(\varphi))]. \tag{A 10}$$

In the case of $\varphi \to 0$, we have $\alpha \to \alpha_0$, $\gamma \to \pi/2$ (cf. figure 18), and then from (A 10)

$$M_2 \to -2a(1 - \sin\alpha_0) \quad \text{for } \varphi \to 0. \tag{A 11}$$

That $\gamma \to \pi/2$ as $\varphi \to 0$, while $\alpha \to \alpha_0$, which may be different from $\pi/2$, on first sight seems to be paradoxical. It assumes a step-like transition from $\gamma = \pi/2$ to $\gamma = \alpha_0 \neq \pi/2$ at the moment when $\varphi$ becomes zero. The reason for that lies in the disappearance of the arcs $BD$ and $AC$ in figure 17 at the moment when $\varphi$ becomes zero and the system attains the configuration shown in figure 16($a$).

For the estimate of $M_1$ note that the dimensionless stress component normal to the plate is of the order of

$$f_n \sim 2\frac{\partial v_n}{\partial n}. \tag{A 12}$$

The velocity gradient estimated at a certain point $B$ on one side of the plate $AB$ is

$$\frac{\partial v_n}{\partial n} \sim \frac{a\omega}{a\varphi} = \frac{\omega}{\varphi}. \tag{A 13}$$

https://doi.org/10.1017/S0022112006004009 Published online by Cambridge University Press

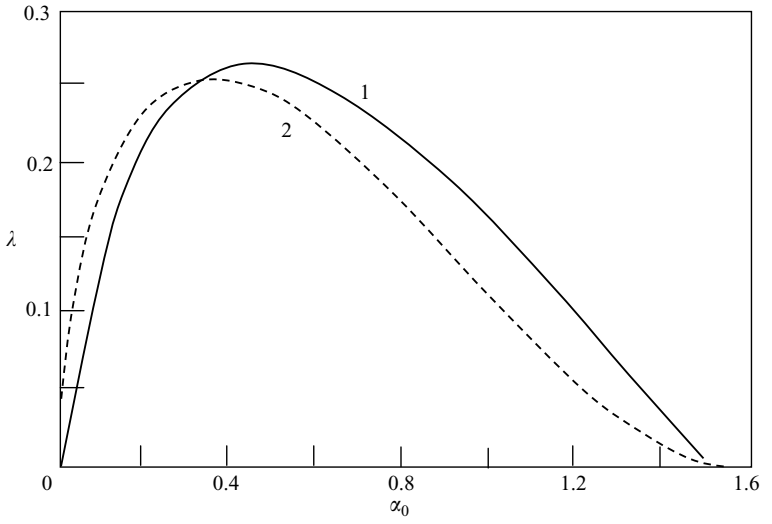



FIGURE 19. Dependence of the decrement $\lambda$ of the exponential attenuation of the angle $\varphi$ on the contact angle $\alpha_0$ of the symmetric static shape shown in figure 16(*a*). Curve 1 corresponds to the dependence found numerically; 2, to the analytical solution.

Then, for $M_1$ of (A 2), we have the following estimate

$$M_1 = -2\int_{-a}^{a} f_n \,\mathrm{d}s \sim -2a^2\frac{\omega}{\varphi} \tag{A 14}$$

(it will be seen that as $\varphi \to 0$, $\omega$ also tends to zero). Equation (A 14) represents only a rough estimate of $M_1$, but the numerical calculations justify it. Substituting (A 11) and (A 14) into (50), we obtain the following equation:

$$\frac{\mathrm{d}^2\varphi}{\mathrm{d}t^2} = -6\beta a\left((1-\sin\alpha_0) + a\frac{1}{\varphi}\frac{\mathrm{d}\varphi}{\mathrm{d}t}\right). \tag{A 15}$$

For $t \to \infty$, when $\varphi \to 0$, equation (A 15) has an approximate asymptotic solution (52) with $\lambda = (1-\sin\alpha_0)/a$ being independent of $\beta$ (i.e. being independent of the plate mass and its geometrical scales, cf. (A 1)). The dependence $\lambda(\alpha_0)$ is shown in figure 19. The dependence (curve 2) has a maximum at $\alpha_0 \approx 0.3$ (17.2°), or $a \approx 2.8$, which means that the characteristic time of the process $T \sim \mu a_0/(\sigma\lambda)$ has a minimum at this value of $a$. Therefore, a certain wetted pad length will result in the fastest alignment of the plate along the pad, and will be optimal in this sense. The two-dimensional calculations allow for an approximate estimate of the optimal length (see figure 19). Note also, that in the three-dimensional case it is difficult to conduct calculations for large values of $a$ (since the number of nodes is strongly restricted by the time consumption for the calculations) to find the dependence $\lambda(a)$.

If the contact lines could move along the plate, then after the moment when the liquid motion has been stopped (just by catching the plate by hand), we should reach a situation where the static contact angle $\alpha_s$ has been achieved at all the contact lines (figure 16*b*). In this case, in the two-dimensional model, $M_1 = M_2 = 0$, and the plate will not move after the moment when we stop holding it, whereas the two-dimensional configuration shown in figure 16(*b*) will continue to be static. Such a static configuration is obviously impossible in the three-dimensional case, where liquid is not totally separated on both sides of $AB$.

https://doi.org/10.1017/S0022112006004009 Published online by Cambridge University Press

## REFERENCES


Becker, A. A. 1992 *The Boundary Element Method in Engineering. A Complete Course*. McGraw-Hill.

Biance, A. L., Clanet, C. & Quere, D. 2004 First steps in the spreading of a liquid droplet. *Phys. Rev.* E **69**, 016301.

Boudreau, A. 1994 Packaging for optoelectronic interconnections. *J. Metals – J. Min. Met. Mat. Sci.* **46**, 41.

Braun, R. J., Murray, B. T., Boettinger, W. J. & McFadden, G. B. 1995 Lubrication theory for reactive spreading of a thin drop. *Phys. Fluids* **7**, 1797–1810.

Cox, R. G. 1986 The dynamics of the spreading of liquids on a solid surface. Part 1. Viscous flow. *J. Fluid Mech.* **168**, 169.

Davis, S. H. 2000 Interfacial fluid dynamics. In *Perspectives in Fluid Dynamics* (ed. G. K. Batchelor, H. K. Moffatt & M. G. Worster), pp. 1–51. Cambridge University Press.

Dimitrakopoulos, P. & Higdon, J. J. L. 1999 On the gravitational displacement of three-dimensional fluid droplets from inclined solid surfaces. *J. Fluid Mech.* **395**, 181.

Drelich, J. & Chibowska, D. 2005 Spreading kinetics of water drops on self-assembled monolayers of thiols: significance of inertial effects. *Langmuir* **21**, 7733.

Dussan V., E. B. 1979 On the spreading of liquids on solid surfaces: Static and dynamic contact lines. *Annu. Rev. Fluid Mech.* **11**, 371.

Gau, H., Herminghaus, S., Lenz, P. & Lipowsky, R. 1999 Liquid morphologies on structured surfaces: from microchannels to microchips. *Science* **283**, 46.

Harsh, K. F., Bright, V. M. & Lee, Y. C. 1999 Solder self-assembly for three-dimensional microelectromechanical systems. *Sensor. Actuat.* A *Phys.* **77**, 237.

Hocking, L. M. 1977 A moving fluid interface. Part 2. The removal of the force singularity by a slip flow. *J. Fluid Mech.* **79**, 209.

Hoffman, R. 1975 A study of advancing interface. I. Interface shape in liquid-gas systems. *J. Colloid Interface Sci.* **50**, 228.

Huang, Y., Duan, X., Wei, Q. & Lieber, C. M. 2001 Directed assembly of one-dimensional nanostructures into functional networks. *Science* **291**, 630.

Kistler, S. F. 1993 Hydrodynamics of wetting. In *Wettability* (ed. L. C. Berg), pp. 311–429. Marcel Dekker.

Landry, K. & Eustathopoulos, N. 1996 Dynamics of wetting in reactive metal/ceramic systems: linear spreading. *Acta Mater.* **44**, 3923.

Lee, Y. C. & Basavanhally, N. 1994 Solder engineering for optoelectronic packaging. *J. Metals – J. Min. Met. Mat. Sci.* **46**, 46.

Lowenberg, M. & Hinch, E. J. 1996 Numerical simulation of a concentrated emulsion in shear flow. *J. Fluid Mech.* **321**, 395.

Messer, B., Song, J. H. & Yang, P. 2000 Microchannel networks for nanowire patterning. *J. Am. Chem. Soc.* B **122**, 10232.

Moffatt, H. K. 1964 Viscous and resistive eddies near a sharp corner. *J. Fluid Mech.* **18**, 1.

Powell, A., Warren, J. & Bailey, C. 1998 Mechanism of motion of an optical fibre aligned by a solder droplet. *MRS Symp. Proc.*

Pozrikidis, C. 1992 *Boundary Integral and Singularity Methods for Linearized Viscous Flow*. Cambridge University Press.

Priede, J., Cramer, A., Gelfgat, A. Y., Bar-Yoseph, P. Z., Yarin, A. L. & Gerbeth, G. 1999 Experimental and numerical study of anomalous thermocapillary convection in liquid gallium. *Phys. Fluids* **11**, 3331.

Rallison, J. M. 1984 The deformation of small liquid drops and bubbles in shear flow. *Annu. Rev. Fluid Mech.* **16**, 45.

Ramanujan, S. & Pozrikidis, C. 1998 Deformation of liquid capsules enclosed by elastic membranes in simple shear flow: large deformations and the effect of liquid viscosities. *J. Fluid Mech.* **361**, 117.

Reznik, S. N. & Yarin, A. L. 2002 Spreading of an axisymmetric viscous drop due to gravity and capillarity on a dry horizontal wall. *Intl J. Multiphase Flow* **28**, 1437.

Reznik, S. N., Zussman, E. & Yarin, A. L. 2002 Motion of an inclined plate supported by a sessile two-dimensional drop. *Phys. Fluids* **14**, 107.


https://doi.org/10.1017/S0022112006004009 Published online by Cambridge University Press

Saiz, E. & Tomsia, A. P. 2004 Atomic dynamics and Marangoni films during liquid-metal spreading. *Nature Mat*. **3**, 903.

Salalha, W., Zussman, E. & Bar-Yoseph, P. Z. 2004 Investigation of flip-chip bonding for MEMS applications. *J. Electron. Packaging* **126**, 48.

Srinivasan, U., Liepmann, D. & Howe, R. T. 2001 Microstructure to substrate self-assembly using capillary forces. *J. Microelectromech. Syst. (JMEMS)* **10**, 17.

Tanner, L. H. 1979 The spreading of silicone oil drops on horizontal surfaces. *J. Phys.* D: *Appl. Phys*. **12**, 1473.

Tummala, R. (ed.) 2001 *Fundamentals of Microsystems Packaging*. McGraw-Hill.

Whitesides, G. M. & Grzybowski, B. 2002 Self-assembly at all scales. *Science* **295**, 2418.

Zinchenko, A. Z., Rother, M. A. & Davis, R. H. 1997 A novel boundary-integral algorithm for viscous interaction of deformable drops. *Phys. Fluids* **9**, 1493.

https://doi.org/10.1017/S0022112006004009 Published online by Cambridge University Press